Monthly Notices of the ROYAL ASTRONOMICAL SOCIETY

Mon. Not. R. Astron. Soc. **407,** 2141–2156 (2010) doi:10.1111/j.1365-2966.2010.17098.x

The primordial non-Gaussianity of local type ($f_{\rm NL}^{\rm local}$) in the *WMAP* 5-year data: the length distribution of CMB skeleton

Zhen Hou,[1,2,3,4]★ A. J. Banday,[2,5] Krzysztof M. Górski,[6,7,8] Franz Elsner[2]
and Benjamin D. Wandelt[9,10]

[1] *Purple Mountain Observatory, Chinese Academy of Sciences, 210008 Nanjing, China*
[2] *Max-Planck-Institute for Astrophysics, Karl-Schwarzschildstrasse 1, D-85741 Garching bei München, Germany*
[3] *Joint Center for Particle, Nuclear Physics and Cosmology, Purple Mountain Observatory – Nanjing University, 210093 Nanjing, China*
[4] *Graduate University of Chinese Academy of Sciences, 100049 Beijing, China*
[5] *Centre d'Etude Spatiale des Rayonnements, 9 av du Colonel Roche, BP 44346, 31028 Toulouse Cedex 4, France*
[6] *Jet Propulsion Laboratory, 4800 Oak Grove Drive, Pasadena, CA 91109, USA*
[7] *California Institute of Technology, Pasadena, CA 91125, USA*
[8] *Warsaw University Observatory, Aleje Ujazdowskie 4, 00-478 Warszawa, Poland*
[9] *Department of Physics, University of Illinois at Urbana-Champaign, 1101 W. Green Street, Urbana, IL 61801-3080, USA*
[10] *Department of Astronomy, University of Illinois at Urbana-Champaign, 1002 W. Green Street, Urbana, IL 61801, USA*

Accepted 2010 May 21. Received 2010 May 21; in original form 2010 March 17

ABSTRACT

We present skeleton studies of non-Gaussianity in the cosmic microwave background temperature anisotropy observed in the 5-yr *Wilkinson Microwave Anisotropy Probe* (*WMAP*) data. The local skeleton is traced on the 2D sphere by cubic spline interpolation which leads to more accurate estimation of the intersection positions between the skeleton and the secondary pixels than conventional linear interpolation. We demonstrate that the skeleton-based estimator of non-Gaussianity of the local type ($f_{\rm NL}^{\rm local}$) – the departure of the length distribution from the corresponding Gaussian expectation – yields an unbiased and sufficiently converged likelihood function for $f_{\rm NL}^{\rm local}$.

We analyse the skeleton statistics in the *WMAP* 5-yr combined V- and W-band data outside the Galactic base-mask determined from the KQ75 sky coverage. The results are consistent with Gaussian simulations of the best-fitting cosmological model, but deviate from the previous results determined using the *WMAP* 1-yr data. We show that it is unlikely that the improved skeleton tracing method, the omission of Q-band data, the modification of the foreground-template fitting method or the absence of six extended regions in the new mask contribute to such a deviation. However, the application of the Kp0 base-mask in data processing does improve the consistency with the *WMAP*1 results.

The $f_{\rm NL}^{\rm local}$-likelihood functions of the data are estimated at nine different smoothing levels. It is unexpected that the best-fitting values show positive correlation with the smoothing scales. Further investigation argues against a point source or goodness-of-fit explanation but finds that about 30 per cent of either Gaussian or $f_{\rm NL}$ samples having better goodness-of-fit than the *WMAP* 5-yr data show a similar correlation. We present the estimate $f_{\rm NL}^{\rm local} = 47.3 \pm 34.9$ (1σ error) determined from the first four smoothing angles and $f_{\rm NL}^{\rm local} = 76.8 \pm 43.1$ for the combination of all nine. The former result may be overestimated at the 0.21σ level because of point sources.

Key words: methods: data analysis – cosmic background radiation.

1 INTRODUCTION

Generic inflationary models predict that the initial conditions of the post-inflation universe can be described by a Gaussian random-phase field with nearly scale-invariant fluctuations. These subsequently seed the perturbations that generate cosmic microwave background (CMB) anisotropies and structure formation thereafter. The Gaussianity of the statistics determined from measures of the CMB anisotropy and large-scale structure distribution can provide evidence that validates the inflationary scenario of the extremely early Universe. Besides the simplest single-scalar field model that

★E-mail: houzhen@pmo.ac.cn

predicts a truly Gaussian initial condition (Guth 1981; Bardeen, Steinhardt & Turner 1983; Mukhanov, Feldman & Brandenberger 1992), there are a number of inflationary models predicting non-Gaussianity in two broad classifications, the *equilateral* type and the *local* type. The detection of a specific type of non-Gaussianity can shed light on the fundamental physical properties of inflation.

In this paper, we are concerned with a *local*-type non-Gaussianity of the 'simplest weak non-linear coupling' case (Komatsu & Spergel 2001):

$$\Phi(\boldsymbol{x}) = \Phi_{\rm L}(\boldsymbol{x}) + f_{\rm NL}^{\rm local}\left[\Phi_{\rm L}^2(\boldsymbol{x}) - \left\langle \Phi_{\rm L}^2(\boldsymbol{x})\right\rangle\right], \tag{1}$$

where $\Phi(\boldsymbol{x})$ denotes the primordial curvature perturbations and $\Phi_{\rm L}$ is its linear Gaussian part. The amplitude of the non-Gaussianity is parametrized by the dimensionless coupling constant $f_{\rm NL}^{\rm local}$ ($f_{\rm NL}$ hereafter). The first observational constraint on $f_{\rm NL}$ – $-3500 < f_{\rm NL} < 2000$ at 95 per cent confidence level (CL) – was discussed by Komatsu et al. (2002) using the angular bispectrum computed from the 4-yr *COBE* DMR data (Bennett et al. 1996). A reduced bispectrum technique, hereafter the KSW estimator (Komatsu, Spergel & Wandelt 2005), was applied to the 1-yr and 3-yr *WMAP* data, leading to $-58 < f_{\rm NL} < 134$ (Komatsu et al. 2003) and $-54 < f_{\rm NL} < 114$ (Spergel et al. 2007), respectively. Yadav & Wandelt (2008) employed an apparently improved estimator (Yadav et al. 2008) to obtain $27 < f_{\rm NL} < 147$ for the $V + W$-band data outside the Kp0 mask with $\ell_{\max} = 750$ with the 3-yr *WMAP* data. The *WMAP* team used the same estimator to measure $f_{\rm NL}$ from the 5-yr *WMAP* $V + W$-band outside the KQ75 mask with $\ell_{\max} = 700$ and obtained $-9 < f_{\rm NL} < 111$.

The possibility of detecting CMB non-Gaussianity using a group of morphological statistics – Minkowski functionals (MFs; Matsubara 2003; Hikage, Komatsu & Matsubara 2006) – has also been studied. The departure of MFs from their Gaussian expectations has been tested to be an unbiased estimator for $f_{\rm NL}$ and then applied to the *WMAP* 3-yr $Q + V + W$ combined map yielding $-70 < f_{\rm NL} < 91$ at the 95 per cent CL (Hikage et al. 2008). The *WMAP* team re-investigated the MFs estimator with the 5-yr template-cleaned $V + W$ map outside the KQ75 mask, yielding $f_{\rm NL} = -57 \pm 60$ (68 per cent CL) at resolution $N_{\rm side} = 128$ and $f_{\rm NL} = -68 \pm 69$ at $N_{\rm side} = 64$ (Komatsu et al. 2009). It is still unclear why the MFs favour a negative best-fitting amplitude for $f_{\rm NL}$ while the bispectrum estimator prefers a positive one, even though the MFs can be formed by the weighted sum of the bispectrum. Thus it is of great importance to use different estimators to identify and investigate the weak non-Gaussian signal in *WMAP* observations. In fact, the one-point probability density function (1-pdf) of the smoothed temperature field can also be implemented (Bernardeau et al. 2002) as an alternative non-Gaussianity estimator (Jeong & Smoot 2007). Indeed, as noted by Novikov, Colombi & Doré (2006), the normalized differential length of the skeleton is closely linked to this quantity, but the skeleton remains of interest due to its different sensitivity to specific aspects of the data, e.g. the noise distribution. It is likely that a complete understanding of the data can only be realized after the application of a wide range of statistical tests.

The skeleton has been considered as a probe of the filamentary structures of a 2D or 3D smooth random field. The original definition of the skeleton is non-local, making the analytical discussion difficult and the numerical evaluation costly. Novikov et al. (2006) first proposed a local approximation that 'the local skeleton is given by the set of points where the gradient is aligned with the local curvature major axis and where the second component of the local curvature is negative'. They also presented a numerical approach to trace the local skeleton and found an approximate expression for the differential length distribution of a Gaussian field. As another morphological statistical test, the method has been applied to both large-scale structure measures (Sousbie et al. 2008a,b) and CMB anisotropies (Eriksen et al. 2004). The latter was performed on the $Q + V + W$ map of the 1-yr *WMAP* data outside a base-mask that is defined on the Kp0 sky coverage. Comparing with Gaussian simulations, the length distribution of the skeleton did not show significant deviation from the Gaussian predictions. The impact of non-excluded point sources was found to be small for the statistics concerned.

In parallel to studies of non-Gaussian signal estimators, several algorithms of simulating non-Gaussian realizations have been developed. Komatsu et al. (2003) first simulated the local-type non-Gaussian component by integrating the spherical harmonics of $\Phi_{\rm L}^2(\boldsymbol{x}) - V_x^{-1}\int {\rm d}^3\boldsymbol{x}\,\Phi_{\rm L}^2(\boldsymbol{x})$ in spherical harmonic space. Another strategy has been developed in which a pre-computed 'filter' encoding the correlation properties of Gaussian curvature perturbation multipoles boosts the computation of high-resolution temperature and polarization Gaussian and corresponding non-Gaussian maps (Liguori, Matarrese & Moscardini 2003; Liguori et al. 2007). This method was recently improved by Elsner & Wandelt (2009). Such $f_{\rm NL}$ simulation methods provide the community with powerful tools to investigate the primordial non-Gaussianity and the impact of other astrophysical and systematic effects on it.

In this paper, the skeleton length distribution is adopted as an estimator of the local-type non-Gaussianity. We adopt the cubic spline interpolation to trace the underlying local skeleton rather than the conventional linear one to make a more accurate estimation of the intersection position between the skeleton and pixel edge. Motivated by MFs studies on $f_{\rm NL}$, the statistical properties of the skeleton length distribution and the convergence of an $f_{\rm NL}$ estimation methodology are investigated from the $f_{\rm NL}$ simulations. We then analyse the skeleton statistics in the 5-yr release of the *WMAP* data and compare with both Gaussian and non-zero $f_{\rm NL}$ samples. The results of the null Gaussian test are compared with those of Eriksen et al. (2004) for the 1-yr *WMAP* data, and then we use the skeleton estimator to compute a likelihood estimate for $f_{\rm NL}$.

This paper is organized as follows. In Section 2, we carry out numerical studies on the CMB local skeleton, including the skeleton statistics utilized in our analysis (Section 2.1) and the test of unbiasedness and convergency of $f_{\rm NL}$ likelihood led by skeleton estimator from noise-free $f_{\rm NL}$ simulations (Section 2.2). Section 3.1 presents an overview of the *WMAP* data and the instrumental properties that should be encoded into our simulations to make an unbiased comparison and parameter estimation. Section 3.2 describes the process of computing the estimator and further analysis from both the observed data and simulations having consistent instrumental properties and sky coverage. Results are reported in Section 4, including the analysis and discussion of a Gaussian frequentist test (Section 4.1) and $f_{\rm NL}$ estimations (Section 4.2). Finally, we present our conclusions in Section 5.

2 NUMERICAL STUDIES ON CMB LOCAL SKELETON

According to the approximation made by Novikov et al. (2006), the local skeleton on a smooth 2D sphere $\rho(\boldsymbol{r})$, traces those points where the gradient of ρ is the eigenvector of the corresponding Hessian matrix. That is, it satisfies the characteristic equation

$$\mathcal{H}\nabla\rho = \lambda\nabla\rho \tag{2}$$

with λ ($\lambda_1 > \lambda_2$; $\lambda_2 < 0$) the eigenvalues, where $\mathcal{H} \equiv \partial^2\rho/\partial r_i \partial r_j$ is the Hessian matrix at position $\boldsymbol{r}$. Identically with Eriksen et al. (2004), we do not specify the condition of eigenvalues of the local linear system. In other words, the skeleton in our analysis is considered as the set of underlying zero-contour lines of the realization:

$$\mathcal{S} = \rho_x \rho_y (\rho_{xx} - \rho_{yy}) + \rho_{xy} \left(\rho_y^2 - \rho_x^2\right), \tag{3}$$

where ρ_i and ρ_{ij} denote the first and second derivatives of $\rho(\boldsymbol{r})$ in two orthogonal directions, x and y. As for the CMB temperature field $T(\boldsymbol{n})$, the 'skeleton map' $\mathcal{S}$ is re-expressed as

$$\mathcal{S} = T_{;\theta} T_{;\phi} (T_{;\theta\theta} - T_{;\phi\phi}) + T_{;\theta\phi} (T_{;\phi}^2 - T_{;\theta}^2), \tag{4}$$

where the semicolons denote the covariant derivatives and the definite expression of them can be found in Schmalzing & Górski (2002).

The method for tracing the local skeleton in the HEALPix scheme has been reviewed in detail by Eriksen et al. (2004). In Appendix A, we seek to optimize the method by applying the cubic spline interpolation for estimating the underlying positions of skeleton 'knots' on the pixelized sphere. The resulting skeleton statistics are introduced and tested for their applicability to non-Gaussian signal detection and $f_{\rm NL}$ estimation.

2.1 The statistics

In this work, the CMB temperature realization intended for skeleton analysis, $T(\boldsymbol{n})$, is first normalized as

$$\nu(\boldsymbol{n}) = \frac{T(\boldsymbol{n})}{\sigma}. \tag{5}$$

The standard deviation σ is computed over the valid region of *each* realization after application of an adequate smoothing process (Section 3.2).

We utilize the skeleton length distribution function of the normalized temperature thresholds ν, as a probe of non-Gaussianity and to construct an estimator of $f_{\rm NL}$. As with any probability density function, there are two types of distributions quantifying the skeleton length, the differential pdf,

$$\mathcal{L}_{\rm d}(\nu) = \frac{1}{L_{\rm tot}} \frac{{\rm d}L(\nu)}{{\rm d}\nu}, \tag{6}$$

and the cumulative one,

$$\mathcal{L}_{\rm a}(\nu) = \int_{\nu}^{+\infty} \mathcal{L}_{\rm d}(\nu')\,{\rm d}\nu', \tag{7}$$

where the normalization factor $L_{\rm tot} = \int_{\nu=-\infty}^{+\infty} {\rm d}L(\nu)$ is the total length.

These two functions are equivalent and should lead to consistent results. In the first investigation of the statistical properties of the skeleton length in the *WMAP* data (Eriksen et al. 2004), the cumulative form was utilized and compared with the predictions of a Gaussian model. In our analysis, both the differential and cumulative functions are computed.

2.2 The idealized skeleton $f_{\rm NL}$ test

We study the signature of the local-type non-Gaussianity as a function of $f_{\rm NL}$ on the skeleton length distributions, $\mathcal{L}_{\rm d}(\nu)$ and $\mathcal{L}_{\rm a}(\nu)$. As a necessary precursor to $f_{\rm NL}$ estimation, we establish that our estimators lead to an unbiased and sufficiently converged $f_{\rm NL}$ likelihood by analysing noise-free full-sky realizations with a non-Gaussian signal component. The test is based on simulations of the CMB anisotropy as a function of $f_{\rm NL}$. We adopt the algorithm proposed by Liguori et al. (2003, 2007) and recently improved by Elsner & Wandelt (2009) to simulate a set of Gaussian realizations ($a_{\ell m}^{\rm G}$) with corresponding non-Gaussian components ($a_{\ell m}^{\rm NG}$). The cosmological parameters adopted for the $f_{\rm NL}$ simulations are those determined for the *WMAP*5 best-fitting Λ cold dark matter (ΛCDM) model (Komatsu et al. 2009). Specifically, the following parameters are adopted: $\Omega_\Lambda = 0.742$, $\Omega_{\rm c}h^2 = 0.1099$, $\Omega_{\rm b}h^2 = 0.02273$, $\Delta_{\mathcal{R}}^2(k_0 = 0.002\,{\rm Mpc}^{-1}) = 2.41 \times 10^{-9}$, $h = 0.719$, $n_{\rm s} = 0.963$ and $\tau = 0.087$. There are a total of 2500 simulated $\{a_{\ell m}^{\rm G}, a_{\ell m}^{\rm NG}\}$ pairs in this test that include power up to a maximum multipole $\ell_{\rm max} = 1024$.

Pixelized sky maps with different $f_{\rm NL}$ values are therefore obtained following the relation:

$$T(p, f_{\rm NL}) = \sum_{\ell=2}^{\ell_{\rm max}} \sum_{m=-\ell}^{\ell} \left(a_{\ell m}^{\rm G} + f_{\rm NL} a_{\ell m}^{\rm NG}\right) b_\ell Y_{\ell m}(p), \tag{8}$$

where b_ℓ is a Gaussian beam transfer function with full width at half-maximum (FWHM) = 30 and 60 arcmin in this test. The first and second derivatives of the map can be computed by the HEALPix routine ALM2MAP_DER. Using the method discussed in Appendix A, the skeleton length distribution $\mathcal{L}(\nu, f_{\rm NL})$ can then be estimated from the skeleton map. In this process, the normalized temperature threshold is set to $\nu \in [-4.0, 4.0]$ with 25 uniform bins.

Given the additive nature of the non-Gaussian component, it is reasonable to express $\mathcal{L}(\nu)$ as

$$\mathcal{L}(\nu, f_{\rm NL}) = \mathcal{L}^{\rm G}(\nu) + \mathcal{L}^{\rm NG}(\nu, f_{\rm NL}). \tag{9}$$

For each $\mathcal{L}(\nu, f_{\rm NL})$ sample, the non-Gaussian component can be estimated as

$$\mathcal{L}^{\rm NG}(\nu, f_{\rm NL}) = \mathcal{L}(\nu, f_{\rm NL}) - \langle \mathcal{L}^{\rm G}(\nu) \rangle, \tag{10}$$

where $\langle \mathcal{L}^{\rm G}(\nu) \rangle$ gives the Gaussian expectation of the skeleton length. We depict the samples of $\mathcal{L}^{\rm NG}(\nu, f_{\rm NL} = 0, \pm 150)$ in Fig. 1. The grey bands indicate the 1σ and 2σ confidence regions of a purely Gaussian ensemble, $f_{\rm NL} = 0$. It is noteworthy that the behaviour of the non-Gaussian expectation values $\langle \mathcal{L}^{\rm NG}(\nu, f_{\rm NL}) \rangle$ for both the differential and cumulative distributions have a characteristic variation with threshold. It is similar to MFs in that the peak–trough order and the amplitude of such features indicate the sign and the magnitude of $f_{\rm NL}$, respectively. This suggests that the skeleton can be considered as another morphological $f_{\rm NL}$ estimator, which may lead to deeper understanding of the underlying non-Gaussian properties of the observations. However, with respect to the 1σ error of $\mathcal{L}^{\rm NG}$, the fluctuation is roughly within the 2σ range of Gaussian predictions, even with $f_{\rm NL} = 150$ which is larger than the 95 per cent CL upper limit for recent $f_{\rm NL}$ estimations using *WMAP* data. It would still be challenging for a skeleton estimator to provide a firm Gaussian/non-Gaussian assessment using the observed data.

Considering only the diagonal elements of the covariance matrix, we use 2000 simulations to estimate $\langle \mathcal{L}^{\rm G}(\nu) \rangle$, the mean and the standard deviation of $\mathcal{L}^{\rm NG}(\nu, f_{\rm NL})$. The 500 remaining simulations are used to compute the χ^2 functions. Given a hypothetical value of $f_{\rm NL}^{\rm true}$, the $\chi^2(f_{\rm NL}|f_{\rm NL}^{\rm true})$ of each $f_{\rm NL}$ skeleton sample with index i ($i = 1, 2, \ldots, 500$) is computed as

$$\chi^2\left(f_{\rm NL}^i | f_{\rm NL}^{\rm true}\right) = \sum_\nu \left[\frac{\mathcal{L}_i^{\rm NG}(\nu, f_{\rm NL}) - \left\langle \mathcal{L}^{\rm NG}\left(\nu, f_{\rm NL}^{\rm true}\right)\right\rangle}{\sigma\left(\mathcal{L}^{\rm NG}\left(\nu, f_{\rm NL}^{\rm true}\right)\right)}\right]^2, \tag{11}$$

where the correlations between bins have not been taken into account because the full covariance matrix is not sufficiently converged for the available sample volume in our analysis. Further

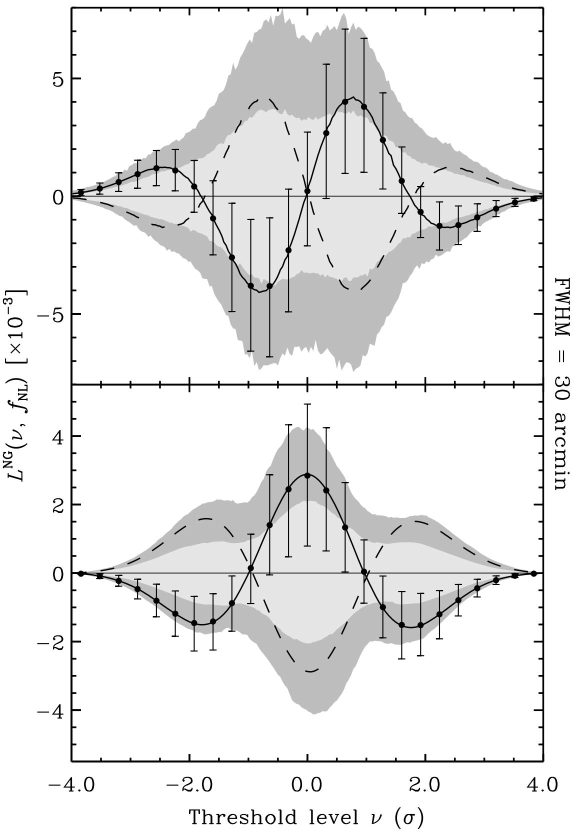

Figure 1. The skeleton estimators obtained from $2500 f_{\rm NL}$ simulations smoothed by a Gaussian beam of FWHM = 30 arcmin. Upper: the differential estimator $\mathcal{L}_{\rm d}^{\rm NG}$. The solid curve depicts the averaged distribution, $\mathcal{L}_{\rm d}^{\rm NG}(\nu, f_{\rm NL} = 150)$, of 200 bins, with the error bars marking the corresponding 1σ errors of the 25 rebinned values (black filled circles), while the dashed curve depicts the estimation of $\langle \mathcal{L}_{\rm d}^{\rm NG}(\nu, f_{\rm NL} = -150)\rangle$. The grey bands correspond to the 1σ (68.26 per cent) and 2σ (95.44 per cent) confidence regions of $\mathcal{L}_{\rm d}^{\rm NG}(\nu, f_{\rm NL} = 0)$, i.e. the Gaussian condition. Lower: the cumulative estimator $\mathcal{L}_{\rm a}^{\rm NG}$. The nomenclature of elements follows the same style as the upper panel.

tests indicate that the corresponding likelihood from each sample is of bimodal or even multimodal shape if the full covariance matrix is adopted, which causes the estimation to be unrevealing.

The parameter $f_{\rm NL}$ is uniformly sampled from −300 to 300 with a step-length $\Delta f_{\rm NL} = 5$. We estimate the likelihoods for three specific $f_{\rm NL}^{\rm true}$ values, 0 and ±150. The posterior PDF for $f_{\rm NL}^{\rm true}$ can be obtained by Bayes' theorem

$$\begin{aligned} P\left(f_{\rm NL}^{\rm true}\Big|\left\{f_{\rm NL}^{i}\right\}\right) &\propto P\left(\left\{f_{\rm NL}^{i}\right\}\Big|f_{\rm NL}^{\rm true}\right)\,P\left(f_{\rm NL}^{\rm true}\right) \\ &\propto \prod_{i=1}^{N} P\left(f_{\rm NL}^{i}|f_{\rm NL}^{\rm true}\right) \\ &\propto \exp\left[-\frac{1}{2}\sum_{i=1}^{N}\chi^2\left(f_{\rm NL}^{i}|f_{\rm NL}^{\rm true}\right)\right], \qquad (12)\end{aligned}$$

where we have conservatively set the prior $P(f_{\rm NL}^{\rm true})$ to be uniform and N equals to 500. In fact, we have found that roughly 20 samples with FWHM = 30 arcmin smoothing are adequate for the posterior distribution to converge sharply around $f_{\rm NL}^{\rm true}$ with a 1σ error $\simeq \Delta f_{\rm NL} = 5$. However, we have only one observed CMB sample so that the convergence of the consequent posterior distribution is limited by the data resolution and the noise level. The effective likelihood functions of each sample, i.e. $\exp[-(1/2N)\sum_{i=1}^{N}\chi^2(f_{\rm NL}^{i}|f_{\rm NL}^{\rm true})]$, are illustrated in Fig. 2, using different normalization factors for visual convenience. The histograms depict the computed likelihoods which are perfectly fitted by Gaussian functions. Accordingly, the mean and the 1σ width of each likelihood are estimated as presented in Table 1.

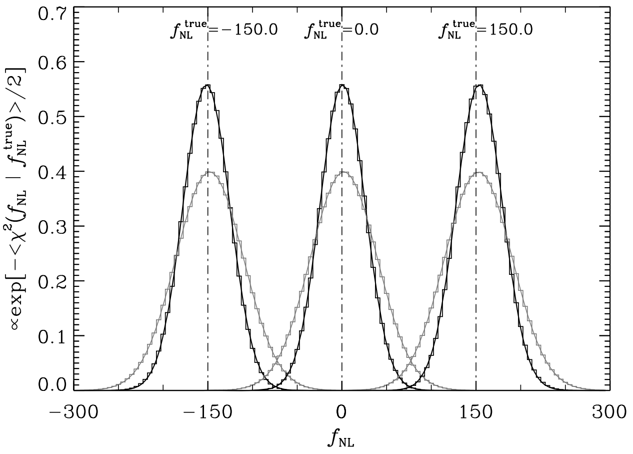

Figure 2. $\exp[-(1/2N)\sum_{i=1}^{N}\chi^2(f_{\rm NL}^{i}|f_{\rm NL}^{\rm true})]$, the effective likelihood functions computed by the differential estimator $\mathcal{L}_{\rm d}^{\rm NG}$ with input parameter $f_{\rm NL}^{\rm true} = 0, \pm 150$. The actual functions are renormalized by different factors for visual convenience and are shown by histograms. They are extremely well fitted by the Gaussian functions depicted by solid curves. The higher, narrower (lower, wider) histograms and curves correspond to likelihoods from simulations with FWHM = 30 arcmin (60 arcmin).

Table 1. The best-fitting $f_{\rm NL}$ and 1σ error from the likelihood $\exp[-(1/2N)\sum_{i=1}^{N}\chi^2(f_{\rm NL}^{i}|f_{\rm NL}^{\rm true})]$ (Fig. 2) computed by differential and cumulative estimators from $N = 500$ noise-free simulations with input parameter, $f_{\rm NL}^{\rm true} = 0, \pm 150$.

Estimator	$f_{\rm NL}^{\rm true}$	$f_{\rm NL}^{\rm best}$		$\sigma_{f_{\rm NL}}$	
		30 arcmin	60 arcmin	30 arcmin	60 arcmin
$\mathcal{L}_{\rm d}^{\rm NG}(\nu, f_{\rm NL})$	−150.0	−151.5	−148.0	26.1	37.8
	0.0	0.8	2.1	25.3	37.5
	150.0	153.6	152.7	26.0	37.8
$\mathcal{L}_{\rm a}^{\rm NG}(\nu, f_{\rm NL})$	−150.0	−151.4	−147.7	23.1	33.5
	0.0	0.7	1.9	22.4	33.2
	150.0	153.2	152.0	23.1	33.5

The results demonstrate a good recovery of the input $f_{\rm NL}$ values given the interval $\Delta f_{\rm NL} = 5$ of our sampling. The $\chi^2(f_{\rm NL}|f_{\rm NL}^{\rm true})$ in equation (11) therefore constitutes an unbiased maximum likelihood (ML) position in $f_{\rm NL}$ space and the corresponding 1σ error is determined by the likelihood function. It is noteworthy that the cumulative estimator behaves a little bit better than the differential one and therefore the former is selected for $f_{\rm NL}$ estimation as applied to real data.

3 METHOD

Even though the literature contains theoretical predictions for the length distributions of the local skeleton on a 2D Gaussian random field, our analysis compares measures derived from simulated observations of the sky with the corresponding values for the *WMAP* data, since the inhomogeneous noise contribution and the complicated sky coverage render analytical investigation difficult. Furthermore, it is also difficult to interpret the non-Gaussian component of

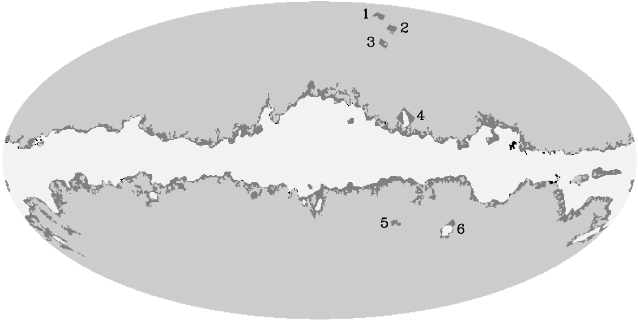

Figure 3. Comparison of the KQ75 base-mask (KQ75B) used in *WMAP*5 data processing with the Kp0 base-mask (Kp0B) used for *WMAP*1 and *WMAP*3 analysis. The white (light grey) regions are excluded (included) by both KQ75B and Kp0B. The dark grey (black) parts are excluded by the former (latter) but not excluded by the latter (former). There are six extended regions (labelled from ‘1’ to ‘6’) eliminated in the KQ75B mask.

these skeleton measures analytically. In what follows, we introduce both the instrumental properties impacting the observed data and the essential numerical processing steps required for further analysis.

3.1 The *WMAP* data and the simulations

The *WMAP* instrument measures the CMB temperature anisotropy in five frequency bands from 23 to 94 GHz (Bennett et al. 2003a). The foreground-reduced sky maps in *V* and *W* band are used in our analysis, identical to the data selection for the *WMAP* 5-yr power spectrum estimation (Nolta et al. 2009). These maps are available in the HEALPix pixelization scheme with $N_{\rm side} = 512$ from the Legacy Archive for Microwave Background Data Analysis (LAMBDA) website.[1] The maps from two (four) differencing assemblies (DAs) at *V* (*W*) band are combined using uniform weights over the sky and equal weights for each DA. The resulting maps in *V* and *W* band are then combined to obtain the *VW*-band map using the same method. The effective beam transfer function of the *VW* band can then be easily computed from the beam functions of those DAs[2] constituting the *VW*-band map. The observational data are inevitably affected by the instrumental noise, dominated by an uncorrelated component with a variance per pixel depending on the noise amplitude σ_0 and the pixel scanning strategies of each DA, $N_{\rm obs}(p)$ (Bennett et al. 2003a).

The extended temperature analysis mask (KQ75) is adopted to minimize the contamination from the diffuse Galactic foreground and point source emission. For further investigations, the part related to the Galactic emission is separated out to form a base-mask called ‘KQ75B’ in our analysis. As a comparison of the base-masks used in the 1-, 3- and 5-yr *WMAP* data analyses, we illustrate the Kp0B (adopted by Eriksen et al. 2004) and KQ75B mask in Fig. 3. Besides the extended Galactic profile, there are six extended regions (labelled from ‘1’ to ‘6’) eliminated by the new base-mask. The impact of these regions on skeleton statistics will be considered when comparing our results with those of Eriksen et al. (2004) for *WMAP*1.

The 2500 pairs of Gaussian and non-Gaussian realizations $\{a_{\ell m}^{\rm G}, a_{\ell m}^{\rm NG}\}$ introduced in Section 2.2 are used for our $f_{\rm NL}$ studies. For each $f_{\rm NL}$ value, we construct a map with resolution parameter $N_{\rm side} = 512$ and *WMAP* instrumental properties as

$$T(p, f_{\rm NL}) = \sum_{\ell=2}^{\ell_{\max}} \sum_{m=-\ell}^{\ell} \left(a_{\ell m}^{\rm G} + f_{\rm NL} a_{\ell m}^{\rm NG}\right) b_\ell p_\ell Y_{\ell m}(p) + \frac{\sigma_0 \eta}{N_{\rm obs}(p)}, \qquad (13)$$

where b_ℓ is the effective beam transfer function of the *WMAP VW*-band data and p_ℓ is the pixelization window function for $N_{\rm side} = 512$. The second term on the right-hand side (rhs) simulates the noise contribution on each pixel with Gaussian random number $\eta \sim N(0, 1)$.

In this work, we perform both a Gaussian frequentist test and $f_{\rm NL}$ estimations. In the former, the Gaussian simulations are processed in the same way as equation (13) but free of the $f_{\rm NL}$ term.

3.2 Data processing and the analysis

In this section, we introduce the data processing methods applied to both the observed and the simulated realizations for studies of the skeleton length distribution. The processing steps presented here follow the strategy detailed in section 4 of Eriksen et al. (2004).

3.2.1 Map processing

The base-mask is applied to the map to avoid Galactic foreground contamination. Following the methodology of Eriksen et al. (2004), we do not exclude point sources, in particular because any additional smoothing applied to the mask reduces the sky coverage available for analysis dramatically. This approach is supported by studies of the spectral parameter, γ, by Eriksen et al. (2004), which indicates that smoothing of the data renders the skeleton less sensitive to point source signal contributions for larger FWHMs. Moreover, a median-filter technique is applied to the point sources to investigate their impact on the skeleton statistics for smaller smoothing FWHMs. Specifically, for a given pixel *i* that would be eliminated by the point-source mask, we consider all other unmasked pixels within a 1° radius and determine the median temperature for this set of pixels. The temperature at pixel *i* is then replaced by this median value, and the process repeated for all pixels specified in the point-source mask. The median-filtered map is then analysed in the same manner as the unfiltered data set.

Following standard procedure in CMB data analysis, the monopole and dipole components are fitted and removed from each map outside the masked region. This step is achieved using the HEALPix F90 subroutine, REMOVE_DIPOLE. The resulting map is then smoothed with a Gaussian beam in harmonic space, again using HEALPix tools. For easy comparison with the previous analysis of Eriksen et al. (2004), the FWHM widths, $\theta_{\rm FWHM}$, selected for these Gaussian smoothing beams are taken to be $0\overset{\circ}{.}53$, $0\overset{\circ}{.}64$, $0\overset{\circ}{.}85$, $1\overset{\circ}{.}28$, $1\overset{\circ}{.}70$, $2\overset{\circ}{.}13$, $2\overset{\circ}{.}55$, $2\overset{\circ}{.}98$ and $3\overset{\circ}{.}40$ (we abandon the larger angular scales used in the former analysis to ensure good convergence of the $f_{\rm NL}$ likelihood). Since a higher resolution map is necessary for more accurate estimation of the skeleton statistics (see Appendix A), the resolution parameter of the resulting smoothed map is set to $N_{\rm side} = 1024$.

After the smoothing of the data, the base-mask must also be expanded and the same processing method is followed. For each smoothing scale, only those base-mask pixels with values larger than 0.99 are defined to be valid pixels on the smoothed mask.

Finally, on the valid region defined by the smoothed base-mask, the map $\tilde{T}(p)$, either from observation or simulation, is

---

[1] http://lambda.gsfc.nasa.gov/product/map/dr3/maps_da_forered_r9_iqu_5yr_get.cfm

[2] http://lambda.gsfc.nasa.gov/product/map/dr3/beam_info.cfm

renormalized to temperature thresholds, ν (equation 5), while the invalid pixels are abandoned for computing the standard deviation. Using the method discussed in Appendix A, the skeleton length distributions, $\mathcal{L}_{\rm d}(\nu)$ and $\mathcal{L}_{\rm a}(\nu)$, can be estimated for each set of smoothed samples. The original distribution $L(\nu)$ in equation (6) is divided into 200 bins with $\nu \in [-4.0, 4.0]$ during skeleton tracing.

3.2.2 *Non-Gaussian detector and estimator*

From the processed Gaussian simulations, we compute the Gaussian expectation of the skeleton statistics for each smoothing scale, $\langle \mathcal{L}^{\rm G}(\nu, \theta_{\rm FWHM})\rangle$. The departure from these expectation values is then obtained for both the observed data and each Gaussian sample as

$$\Delta\mathcal{L}(\nu, \theta_{\rm FWHM}) = \mathcal{L}(\nu, \theta_{\rm FWHM}) - \left\langle \mathcal{L}^{\rm G}(\nu, \theta_{\rm FWHM})\right\rangle, \qquad (14)$$

and the corresponding χ^2 value is then computed:

$$\chi^2 = \left[\frac{\Delta\mathcal{L}(\nu, \theta_{\rm FWHM})}{\sigma(\Delta\mathcal{L}(\nu, \theta_{\rm FWHM}))}\right]^2, \qquad (15)$$

where we omit the $\langle \Delta\mathcal{L}\rangle$ term since it is definitely zero. In the $f_{\rm NL}$ analysis, the non-Gaussian departure, $\mathcal{L}^{\rm NG}(\nu, f_{\rm NL}, \theta_{\rm FWHM})$, and the χ^2 statistics are estimated by equations (10) and (11). The best-fitting value and error of $f_{\rm NL}$ can then be obtained by analysing the likelihood function as discussed in Section 2.2.

Before we provide final estimates of $f_{\rm NL}$ from the different smoothing scales, we combined the estimators, $\Delta\mathcal{L}(\nu)$ of the data and $\mathcal{L}^{\rm NG}(\nu, f_{\rm NL})$ of each set of $f_{\rm NL}$ sample, to

$$\Delta\mathcal{L}_{\rm C}(\nu, f_{\rm NL}) = \sum_{i=1}^{N_{\rm FWHM}} w_i(\nu, f_{\rm NL})\Delta\mathcal{L}^i(\nu) \qquad (16)$$

and

$$\mathcal{L}_{\rm C}^{\rm NG}(\nu, f_{\rm NL}) = \sum_{i=1}^{N_{\rm FWHM}} w_i(\nu, f_{\rm NL})\mathcal{L}^{{\rm NG},i}(\nu, f_{\rm NL}), \qquad (17)$$

respectively, with the inverse-variance weighting

$$w_i(\nu, f_{\rm NL}) = \frac{1/\sigma^2\left(\mathcal{L}^{{\rm NG},i}(\nu, f_{\rm NL})\right)}{\sum_{i=1}^{N_{\rm FWHM}} 1/\sigma^2\left(\mathcal{L}^{{\rm NG},i}(\nu, f_{\rm NL})\right)}, \qquad (18)$$

where i corresponds to one smoothing scale and $N_{\rm FWHM}$ represents the number of scales used in the combination. The combined χ^2 is then computed:

$$\chi^2_{\rm C}(f_{\rm NL}) = \sum_\nu \left\{\frac{\Delta\mathcal{L}_{\rm C}(\nu, f_{\rm NL}) - \left\langle \mathcal{L}_{\rm C}^{\rm NG}(\nu, f_{\rm NL})\right\rangle}{\sigma\left[\mathcal{L}_{\rm C}^{\rm NG}(\nu, f_{\rm NL})\right]}\right\}^2. \qquad (19)$$

This combination makes an integrated estimation of $f_{\rm NL}$ which includes the non-Gaussian signal at several different scales with a mild weighting.

4 RESULTS AND DISCUSSIONS

4.1 Gaussian frequentist results

We first compare the observed results with our Gaussian model predictions. In this case, we perform 10 240 Gaussian simulations of the *WMAP VW*-band properties. Different base-masks, as well as the median filter, are applied independently to both the real and the simulated skies to study the foreground effect on the skeleton results. The corresponding χ^2 values are then computed to enable the frequentist test.

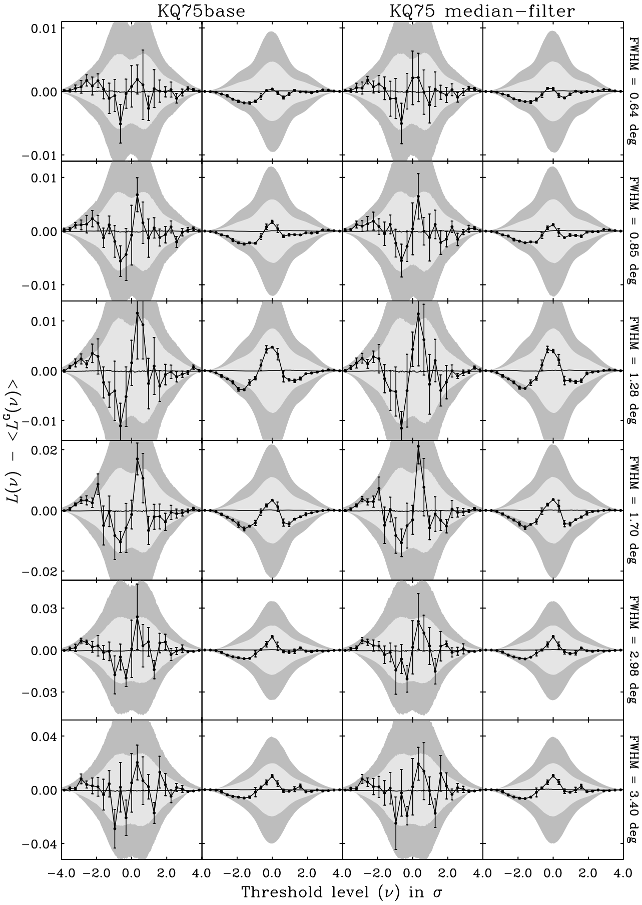

Figure 4. The skeleton statistics, $\Delta\mathcal{L}(\nu) = \mathcal{L}(\nu) - \langle \mathcal{L}^{\rm G}(\nu)\rangle$, computed from KQ75B (left two columns) and KQ75 median filter (right two columns) processing on smoothing scales FWHM = $0\overset{\circ}{.}64$, $0\overset{\circ}{.}85$, $1\overset{\circ}{.}28$, $1\overset{\circ}{.}70$, $2\overset{\circ}{.}98$ and $3\overset{\circ}{.}40$. The first and third columns (the second and forth columns) correspond to results of the differential (cumulative) estimator. The grey bands show the 1σ and 2σ confidence regions defined by 10 240 Gaussian samples. The black filled circles connected by solid lines show the observed sample which is rebinned to 25 bins. The error bar mark the 1σ error in each bin according to such rebinning.

4.1.1 *Results of KQ75B processing*

For each smoothing scale, the skeleton length departure from the Gaussian expectation, $\Delta\mathcal{L}(\nu, \theta_{\rm FWHM}) = \mathcal{L}(\nu, \theta_{\rm FWHM}) - \langle \mathcal{L}^{\rm G}(\nu, \theta_{\rm FWHM})\rangle$, is computed from samples obtained with the KQ75B masked maps. The results are shown in the left two columns (for both the differential and cumulative distributions) of Fig. 4 for $\theta_{\rm FWHM} = 0\overset{\circ}{.}64$, $0\overset{\circ}{.}85$, $1\overset{\circ}{.}28$, $1\overset{\circ}{.}70$, $2\overset{\circ}{.}98$ and $3\overset{\circ}{.}40$. The grey bands demonstrate the 1σ and 2σ confidence regions of the Gaussian prediction. The observed ones are rebinned to 25 bins and depicted by filled circles with the 1σ error bar of each bin. The rebinning is necessary since the differential skeleton distribution is relatively noisy.

In the case of the cumulative distributions, $\Delta\mathcal{L}_{\rm a}(\nu)$ for *WMAP*5, some features consistent with a positive $f_{\rm NL}$ value are observed, albeit within the 1σ Gaussian confidence level. The behaviour of the differential distribution, $\Delta\mathcal{L}_{\rm d}(\nu)$, supports this inference despite the existence of a higher level of fluctuations. However, there are differences between the new results and the corresponding *WMAP*1 ones (Eriksen et al. 2004). For each smoothing scale, the latter show a 1σ-level peak around $\nu = 0$ while the neighbouring troughs

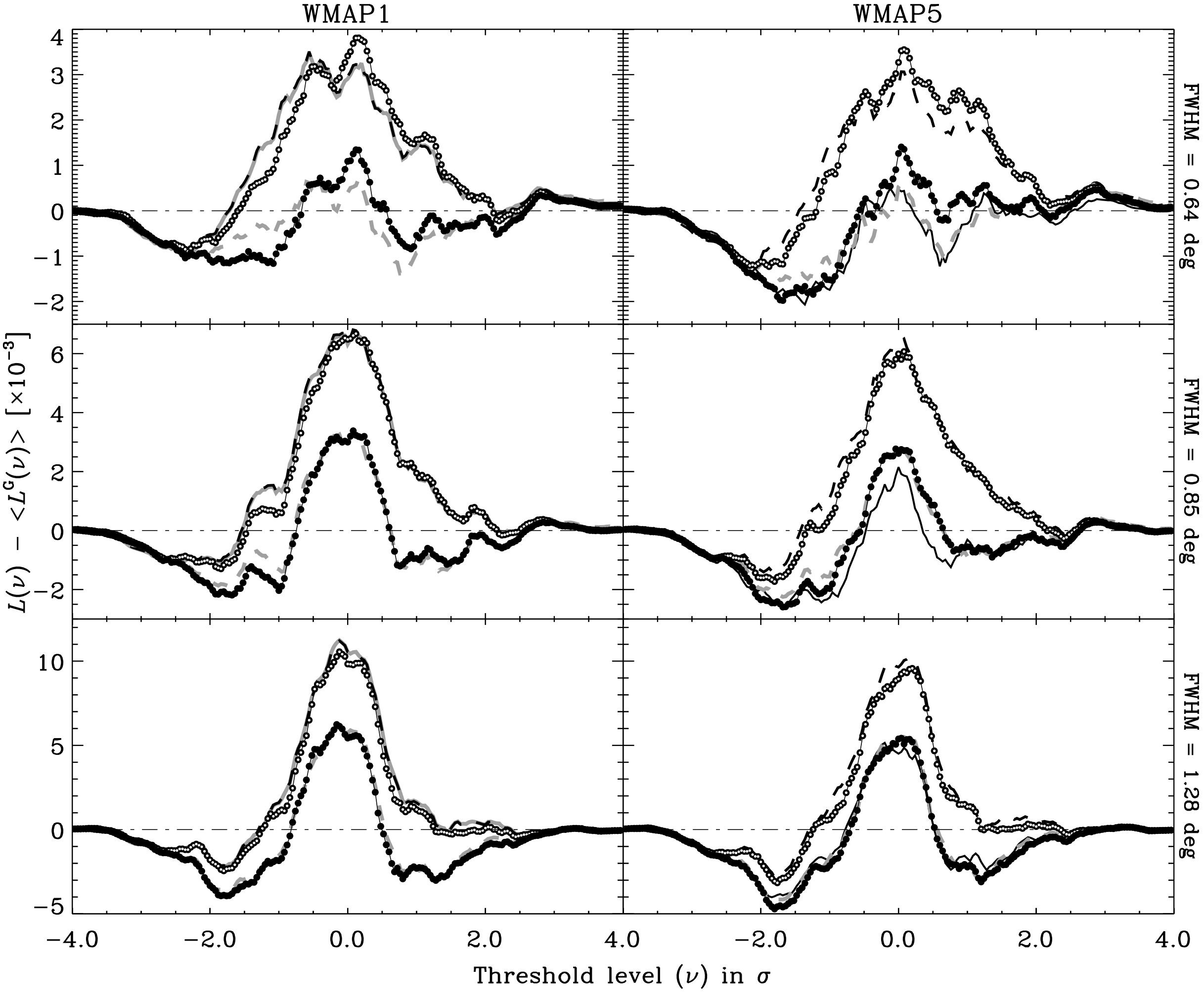

Figure 5. The skeleton statistics, $\Delta\mathcal{L}_a(\nu)$, computed from different processing methods. Left-hand column: the results obtained from the 1-yr *WMAP* data. Right-hand column: the results obtained from the 5-yr *WMAP* data. The lines and symbols denoting different processing elements are noted in Table 2.

show less fluctuations especially in the $\nu > 1$ region. In contrast, as shown in Fig. 4 (the left two columns), the former's peak is less apparent but the troughs are much more distinct particularly for $\theta_{\rm FWHM} = 1\overset{\circ}{.}28$ and $1\overset{\circ}{.}70$. The comparison between *WMAP*1 and our new results is shown in Fig. 5 for $\theta_{\rm FWHM} = 0\overset{\circ}{.}64$, $0\overset{\circ}{.}85$ and $1\overset{\circ}{.}28$. The lines and symbols in the figure are noted in Table 2 denoting different processing elements.

There are several possibilities associated with such a discrepancy.

(1) *Change of the skeleton-tracing method.* Utilizing cubic spline interpolation in the skeleton-tracing algorithm yields a more accurate estimation of the quantities than the previously adopted linear algorithm (see Appendix B). We computed $\Delta\mathcal{L}_a(\nu)$ for the template-cleaned *WMAP*1 data using the same band selection, mask and processing steps as in Eriksen et al. (2004), and tracing the underlying skeleton by both linear and cubic spline interpolation strategies. The Gaussian expectation is also estimated in both cases using simulations. The results are shown in the left column of Fig. 5 where it can be seen that the dashed black line (cubic spline) and the solid grey line (linear) essentially overlap. It is therefore clear that changing the interpolation scheme contributes little to the discrepancy found. This issue is also discussed in Appendix B for the *WMAP*5 data.

Table 2. The processing elements for the styles of lines and symbols in Fig. 5.

Band	Mask[a]	Fore red[b]	Interp[c]	Style
QVW	Kp0B	1 yr	Cubic	Dashed black line
QVW	Kp0B	5 yr	Cubic	Connected open circles
QVW	KQ75B	1 yr	Cubic	Dashed grey line
QVW	KQ75B	5 yr	Cubic	Connected filled circles
QVW	Kp0B	1 yr	Linear	Solid grey line
VW[d]	KQ75B	5 yr	Cubic	Solid black line

[a] The base-mask applied in map processing and analysis.
[b] The templates and the corresponding coefficients applied for foreground reducing before our map processing.
[c] The interpolation method used for tracing the underlying local skeleton.
[d] The $V + W$ combined data with uniform weighting, while spatial invariant inverse-noise-variance weighting for *QVW*.

(2) *Band selection.* In the analysis of Eriksen et al. (2004), the *Q*-, *V*- and *W*-band maps are combined with a spatially invariant inverse-noise-variance weighing. The resulting map is dominated by the *Q* band since it has the lowest noise of the three. However, since it is the band for which Galactic foreground residuals remain significant, it is plausible that these have an impact on the

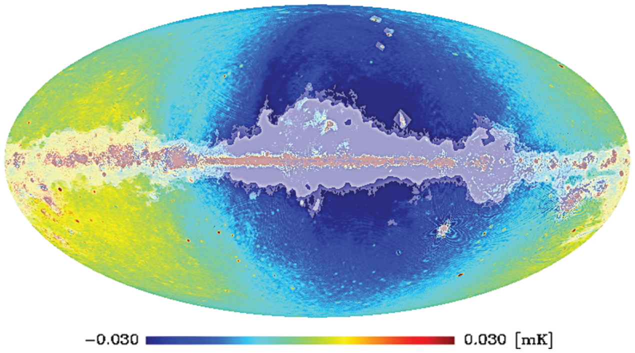

Figure 6. The difference map between the *WMAP*1 and *WMAP*5 combined foreground models at *V* band, between *WMAP*1 and *WMAP*5. The Kp0B and KQ75B masks are also denoted. The ringing effect around some bright sources, especially the Large Magellanic Cloud (LMC), comes from the 1-yr processing of the three templates (Bennett et al. 2003b).

skeleton results. We repeated our analysis using the appropriately weighted *WMAP*5 *Q*-, *V*- and *W*-band data, but retaining the KQ75B base-mask. Corresponding Gaussian simulations are also performed. The results are shown as the black connected filled circles in the right-hand column of Fig. 5. The profile shows modest deviation from our VW results (solid black line), however, it does not result in the discrepancy level required. On the contrary, the difference becomes less significant for large $\theta_{\rm FWHM}$.

(3) *Difference of the foreground subtraction method between WMAP1 and WMAP5.* The foreground templates used for the former (Bennett et al. 2003b) are the FDS 94 GHz dust prediction, the Hα map for free–free emission and the 408-MHz Haslam map for synchrotron emission. The 3-yr *WMAP* foreground analysis (Hinshaw et al. 2007) and beyond replace the 408-MHz data with a template based on the K–Ka difference map. The difference between the two foreground models at *V* band utilizing the coefficients for the 1-yr fits of Bennett et al. (2003b) and the 5-yr analysis of Gold et al. (2009) is shown in Fig. 6. The profile demonstrates a dipole-like structure in the large-scale temperature distribution outside both the Kp0B or KQ75B masks, which may affect the skeleton statistics and the corresponding inferences of $f_{\rm NL}$. We subtract the 5-yr foreground model from the 1-yr raw maps at *Q*, *V* and *W* bands, which are then combined and processed identically with Eriksen et al. (2004) using the Kp0B mask. The corresponding skeleton statistic, $\Delta\mathcal{L}_{\rm a}(\nu)$, is depicted by the connected open circles in the left-hand column of Fig. 5. They demonstrate consistency with the original *WMAP*1 results. Similarly, another independent test has been carried out on the 5-yr raw maps from which the 1-yr foreground model is subtracted before the data are combined and processed using the KQ75B mask. The results are depicted as the dashed grey line in the right-hand column of Fig. 5, and demonstrate consistency with our 5-yr templated-cleaned *VW*-KQ75B results (solid black line). We conclude that it is difficult to attribute the observed discrepancy to the change of foreground subtraction method.

(4) *Change of the base-mask in processing.* It is very suspicious that the residual foreground components around the dark-grey regions in Fig. 3 bias the skeleton results of *WMAP*1, although mild smoothing and mask thresholding are applied before skeleton tracing. We discuss this issue in Section 4.1.2 by investigating the Galactic plane region and the extragalactic sources (labelled from 1–6 in Fig. 3) separately.

As shown by the left two columns in Fig. 4, the profile of the *WMAP*5$\Delta\mathcal{L}_{\rm a}(\nu)$ function is consistent with that expected for a positive $f_{\rm NL}$. In particular, both $\Delta\mathcal{L}_{\rm d}$ and $\Delta\mathcal{L}_{\rm a}$, rebinned for FWHM = 1°.28 and 1°.70, demonstrate consistent features with the solid lines shown in Fig. 1 for $f_{\rm NL} = +150$. However, the troughs in the $\nu > 1$ region (hot region) seem relatively less depressed. It is likely that the point sources and foreground components contribute to this asymmetry between the two troughs. The results from the median-filtered map yield insights implications into this issue.

Table 3. The χ^2-based frequentist results for the *WMAP*5 skeleton analysis derived using different processing masks and methods on 10 smoothing scales. We list the fraction of the simulations with a χ^2 values less extreme than the observed one. The letters 'M' correspond to 'median filter'. The values are determined from the estimator $\Delta\mathcal{L}_{\rm a}(\nu)$ computed for 200 bins from the data and 10 240 Gaussian samples. The corresponding results for *WMAP*1 (Eriksen et al. 2004) are also listed for easy comparison.

FWHM	*WMAP*1	KQ75B	KQ75M	Kp0B	KQhybrid
0°.53	0.234	0.1220	0.1115	0.0812	0.1310
0°.64	0.286	0.1503	0.1345	0.1539	0.1604
0°.85	0.354	0.2608	0.2148	0.2147	0.2720
1°.28	0.293	0.3490	0.3167	0.2481	0.3590
1°.70	0.284	0.4258	0.3761	0.1360	0.4504
2°.13	0.248	0.3691	0.3745	0.1669	0.3822
2°.55	0.208	0.3205	0.3352	0.1379	0.3361
2°.98	0.166	0.2728	0.2684	0.1343	0.2892
3°.40	0.113	0.2119	0.2389	0.1023	0.2237
3°.83	0.081	0.1866	0.2410	0.0923	0.1963

We computed the χ^2 values of $\Delta\mathcal{L}_{\rm a}$ for both the observed and the simulated samples. We list the fraction of the simulations with a χ^2 values less extreme than the observed one in Table 3. The corresponding *WMAP*1 results are also listed (table 3 in Eriksen et al. 2004). Generally speaking, there is no qualitative difference between the 5- and 1-yr results. However our results show a unimodal dependence on the smoothing scales. The $f_{\rm NL}$ signal seems more significant around the angular scales FWHM = 1°.28, 1°.70 and 2°.13.

4.1.2 *Results of Kp0B and KQhybrid processing*

We applied the 1-yr Kp0B mask used in Eriksen et al. (2004) in our analysis with all other operations remaining unchanged. We also create a new base-mask called 'KQhybrid' which excludes the same Galactic plane with KQ75B but handles the six extended sources (Fig. 3) identically to Kp0B. The KQhybrid mask is then included in the data processing too as an independent test. Some of the results are shown in Fig. 7 and the right-hand column of Fig. 5.

In general, the $\Delta\mathcal{L}_{\rm a}$ profiles of the Kp0B processing are generally consistent with the previous *WMAP*1 results, although the peak–trough structure is not identical in detail. The KQhybrid mask yields a consistent set of results with those of KQ75B as shown in Fig. 7. Moreover, we have applied the KQ75B mask to the *WMAP*1 data and found that the results (dashed grey line in the left-hand column of Fig. 5) show a similar discrepancy from the Kp0B processed ones and consistency with results from our 5-yr *VW* data processing. This indicates that modifications of the mask do significantly affect the skeleton estimation in the *WMAP*1 analysis. Although the reason can be easily found by examining the area ratio of the dark-grey regions in Fig. 3, it is important to make a separate investigation on the impact of residual Galactic foreground and extragalactic sources since $f_{\rm NL}$ analysis exhibits different responses to different types of foreground contamination (Cabella et al. 2010). This separate

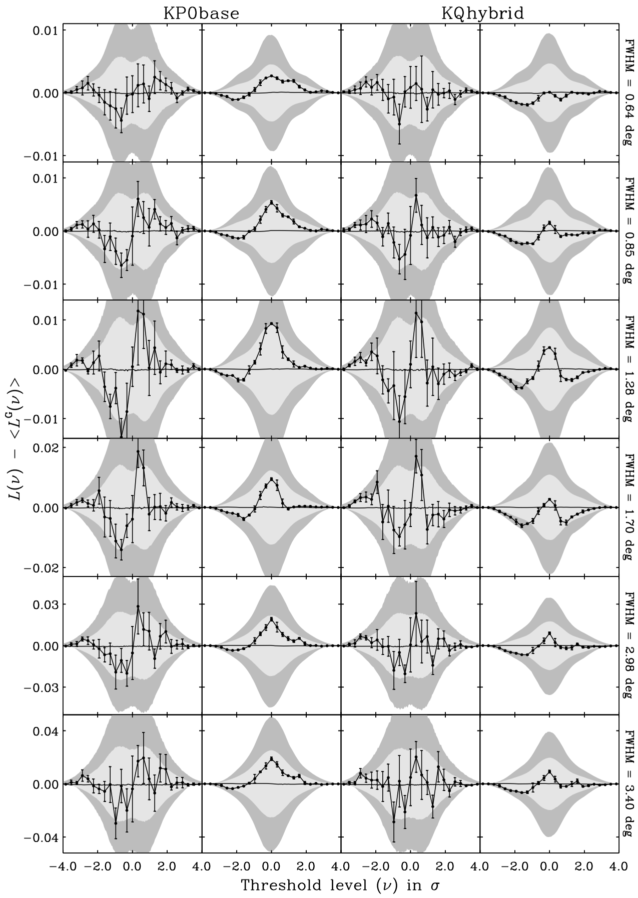

Figure 7. The skeleton statistics, $\Delta\mathcal{L}(\nu) = \mathcal{L}(\nu) - \langle\mathcal{L}^{\rm G}(\nu)\rangle$, computed from Kp0B (left two columns) and KQhybrid (right two columns) processing on smoothing scales FWHM = 0°.64, 0°.85, 1°.28, 1°.70, 2°.98 and 3°.40. The nomenclature of the elements follows the same style as Fig. 4.

analysis motivates future skeleton studies on the effects of different Galactic foreground templates.

It is noteworthy that the skeleton discrepancies caused by base-mask selection indicate that residual Galactic foregrounds bias the non-Gaussian analyses for *WMAP*1 and even *WMAP*3 since the Kp0 mask was the standard temperature analysis window then and the Kp2 mask excluded even less area around Galactic plane. This issue may have implications on the bispectrum analysis because the additional smoothing operation, which smears the local structures of foreground templates, is not necessary for bispectrum estimation.

The foreground issue is also assessed as a complement to the mask-changing analysis. We subtracted the 5-yr (1-yr) foreground templates from the raw maps of *WMAP*1 (*WMAP*5) data. The subtracted maps are then combined and processed using the KQ75B (Kp0B) mask and the skeleton results are depicted as the connected filled circles (dashed black line) in the left-hand (right-hand) column of Fig. 5. They are consistent with the results from the standard foreground subtraction processing with the same corresponding base-mask. It is therefore confirmed that the foreground model is not responsible for the discrepancy of the skeleton statistics as seen.

The corresponding results are listed in Table 3. It is straightforward to infer that the KQhybrid processing results are more consistent with the corresponding KQ75B ones. The differences of a few per cent come from the six extended regions. The χ^2 results from the Kp0B processing are somewhat different to the *WMAP*1 inference although the profiles of $\Delta\mathcal{L}_{\rm a}$ are quite similar. Besides the band selection, it is most probably due to the modified template fitting of the Galactic foreground in 5-yr data processing, as well as the better signal-to-noise ratio (S/N) level in 5-yr data.

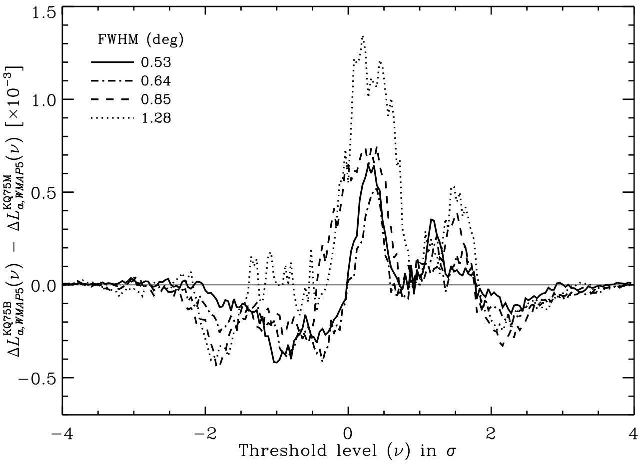

Figure 8. The distribution difference between KQ75B and KQ75 median filter processed estimator, $\Delta\mathcal{L}_{\rm a}$ of *WMAP*5 data. The cases of different smoothing scales are distinguished by different line styles.

4.1.3 *Results of median-filter processing*

In order to assess the validity of the results from the KQ75B mask analysis in which point sources are not excluded, we have applied a median filter to those pixels located at positions in the point source mask before smoothing, then processed the filtered map to obtain the skeleton statistics. Some results are plotted in the right two columns of Fig. 4, and listed in Table 3. In general, the median filtered results show good consistency with the KQ75B results even for the first few smoothing scales, implying that the base-mask processing is safe for skeleton analysis on the scales considered in this work.

Nevertheless, small visual differences suggest further investigation into how point sources modify the skeleton statistics and the $f_{\rm NL}$ estimations. We make a comparison of the *WMAP* 5 $\Delta\mathcal{L}_{\rm a}$ between the KQ75B and median-filter processing. The differences between them are plotted in Fig. 8 for FWHM = 0°.53, 0°.64, 0°.85 and 1°.28 by solid, dot–dashed, dashed and dotted lines, respectively. It is suggested that the point sources do have asymmetric impacts on the skeleton for positive and negative temperature thresholds – negative biasing is seen for the range $-2.0 < \nu < 0.0$ and positive biasing is apparent for $0.0 < \nu < 2.0$. In particular for the dotted line, a 30 per cent lower depression is observed over $0.0 < \nu < 0.5$. This could bias the best-fitting $f_{\rm NL}$ value though the bins around this range are assigned lower weights according in the combined χ^2 computation. Although the plot suggests that the magnitude of potential biasing seems to increase with smoothing scale, the larger smoothing still reduces sensitivity to point sources. Moreover, the profiles seen in Fig. 8 become increasingly noise like within the range $\nu \in [-2.5, 2.5]$ at larger smoothing scales.

4.2 $f_{\rm NL}$ estimation

4.2.1 *General results*

Using the method introduced in Section 2.2, the likelihood function for $f_{\rm NL}$ is estimated for each smoothing scale based on the 2500 sets of $f_{\rm NL}$ samples, $\mathcal{L}^{\rm NG}(\nu, \{f_{\rm NL}\})$. We sample the parameter within the range $f_{\rm NL} \in [-200, 400]$ with step-length $\Delta f_{\rm NL} = 2.5$. The KQ75B-processed data are utilized from FWHM = 0°.53 to 3°.40 with the median-filter-processed data from FWHM = 0°.53 to 1°.28 compared for reference. We use the cumulative estimator $\Delta\mathcal{L}_{\rm a}$ because it leads to 10 per cent more converged estimations than the differential one according to a mock test (Section 2.2). Before χ^2 computation, the estimator resulting from both the observed data and simulations are rebinned to 25 bins.[3]

The results are shown in the top panel of Fig. 9 with each curve depicting the likelihood (without normalization) for each smoothing scale. The likelihood functions are fitted by Gaussian functions so that the best-fitting $f_{\rm NL}$ and the corresponding 1σ error are obtained and then marked in the same plot. The likelihood at the highest resolution indicates that the Gaussian hypothesis ($f_{\rm NL} = 0$) is rejected only at 0.8σ level, while it increases to 2.7σ for FWHM = 2°.13. It is apparent that the best-fitting $f_{\rm NL}$ values show a positive correlation with the smoothing scale, which is unexpected since $f_{\rm NL}$ is scale independent according to the local-type non-Gaussian model and our simulations.

As discussed in Section 4.1.3, although the estimation is inevitably biased by the point sources or other types of foreground, large angle smoothing renders the estimation insensitive to those effects. We repeat the estimation using median-filtered samples from the first four smoothing scales. As shown in the middle panel of Fig. 9, the results are consistent in general, and the positive correlation between $f_{\rm NL}^{\rm best}$ and the smoothing scales is identical to the unfiltered analysis. It is therefore suggested that the point sources contribute little to such correlation. The 1σ errors are robust according to the median-filter reference but the best-fitting values of $f_{\rm NL}$ from the KQ75B processing seem to be overestimated by levels of 0.04σ, 0.26σ, 0.39σ and 0.22σ for FWHM = 0°.53, 0°.64, 0°.85 and 1°.28, respectively.

In principle, different heights of the likelihoods represent variations in the goodness-of-fit if the corresponding χ^2 values have the same number of degrees-of-freedom. A higher likelihood implies the $f_{\rm NL}$ expectation fits the data better and it does appear that the likelihoods from larger angle smoothing (FWHM = 2°.55, 2°.98 and 3°.40) show better results than for smaller FWHMs. However, in our analysis, we pick up only the diagonal elements of the covariance matrix to compute the χ^2. It is inappropriate to make a theoretical interpretation of the goodness-of-fit. Consequently, the correlation found above would be a false appearance because there might be some bad fittings. For each FWHM, the χ^2 value at the ML of the *data* is represented as $\chi^2_{\rm min}$. Accordingly, there are 2500 sampled $\chi^2(\{f_{\rm NL}\}\,|f_{\rm NL}^{\rm ML})$ and each has a minimum within our sampling range. We count the probability of $\chi^2_{\rm min}(\{f_{\rm NL}\}|f_{\rm NL}^{\rm ML}) < \chi^2_{\rm min}$ to quantify the goodness-of-fit for results from both the KQ75B and median-filter processing, with a lower probability corresponding to a better fit. The $\chi^2_{\rm min}$ values and the probabilities are listed in Table 4. The moderate probabilities are consistent with each other though they may be underestimated for the last three FWHMs. On one hand, it is demonstrated that our skeleton statistic fits the possible $f_{\rm NL}$ feature in the *WMAP*5 data and our estimations are therefore validated. On the other hand, it remains unconfirmed what the source of the positive correlation between $f_{\rm NL}^{\rm best}$s and smoothing scales is, and which we will return to in Section 4.2.3.

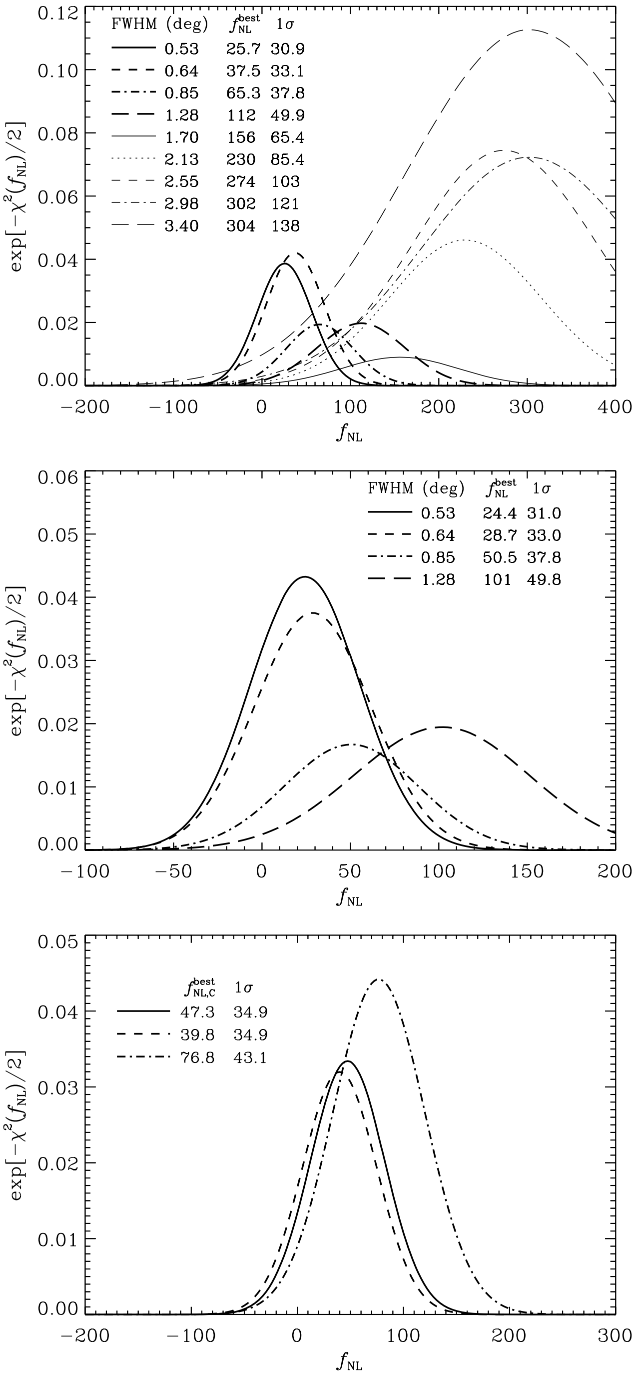

Figure 9. The likelihood functions of $f_{\rm NL}$ from the skeleton statistic for *WMAP*5 data. Top: the $f_{\rm NL}$ likelihood functions computed by KQ75B processed $\Delta\mathcal{L}_{\rm a}(\nu)$ and $\mathcal{L}_{\rm a}^{\rm NG}(\nu, f_{\rm NL})$ on nine different smoothing scales. The estimator is rebinned to 25 bins before analysis. The best-fittings and 1σ errors are obtained by fitting the likelihoods using Gaussian functions. Middle: similar cases for statistic derived by KQ75 median-filter processing on four smoothing scales. Bottom: the $f_{\rm NL}$ likelihood functions estimated from the combined estimator $\Delta\mathcal{L}_{a,{\rm C}}(\nu, f_{\rm NG})$ and $\mathcal{L}_{\rm a}^{\rm NG}(\nu, f_{\rm NG})$. The solid (dot–dashed) curve shows the likelihood computed from KQ75B processed estimator with four (nine) FWHMs combined. The dashed curve corresponds to the KQ75 median-filter processed likelihood.

4.2.2 Estimation from the combined $\Delta\mathcal{L}_{\rm a}$

As presented in Section 3.2.2, the combinations on different smoothing scales are applied separately to the rebinned $\Delta\mathcal{L}_{\rm a}(\nu)$ of the data

---

[3] It has been tested that 25 is the best number for rebinning in our analysis. More bins will make the estimator more noisy so that the resulting likelihood is bimodal or even multimodal, whereas less bins will make the likelihood less converged.

Table 4. The goodness-of-fit, i.e. the probabilities that the simulated samples with $\{\chi^2_{\rm min}(f_{\rm NL}|f_{\rm NL}^{\rm ML})\} < \chi^2_{\rm min}$. $f_{\rm NL}^{\rm ML}$ and $\chi^2_{\rm min}$ are the maximum likelihood $f_{\rm NL}$ of the data and its corresponding χ^2 value of each case, respectively. The results in the case of combined data (KQ75B Comb.) are also listed.

FWHM	KQ75B		KQ75M		KQ75B Comb.	
	$\chi^2_{\rm min}$	P (per cent)	$\chi^2_{\rm min}$	P (per cent)	$\chi^2_{\rm C,min}$	P (per cent)
0°.53	6.50	27.1	6.28	20.9	6.80	30.4
0°.64	6.34	25.8	6.57	22.3		
0°.85	7.89	35.6	8.18	30.5		
1°.28	7.85	33.5	7.88	27.3		
1°.70	9.42	40.5	N/A	N/A	6.24	28.0
2°.13	6.15	19.5	N/A	N/A		
2°.55	5.20	12.1[a]	N/A	N/A		
2°.98	5.26	11.7	N/A	N/A		
3°.40	4.37	6.0	N/A	N/A		

[a] This number may be underestimated because the underlying χ^2 minima of some samples lay outside our $f_{\rm NL}$ sampling range, i.e. their corresponding $f_{\rm NL}^{\rm ML} > 400$. Similar cases are also found for FWHM = 2°.98 and 3°.40.

and $\mathcal{L}_{\rm a}^{\rm NG}(\nu,\, f_{\rm NL})$ of the $f_{\rm NL}$ samples. It is verified that such a combination still leads to an unbiased estimation of $f_{\rm NL}$ (Appendix C).

In our analysis, the first four and all nine scales are combined, yielding estimates of $f_{\rm NL,C} = 47.3 \pm 34.9$ and 76.8 ± 43.1, respectively, by fitting the likelihood using a Gaussian function. The likelihoods are shown in the bottom panel of Fig. 9 and the goodness-of-fit is listed in Table 4. The estimates are consistent with the results discussed in Section 4.2.1 and the moderate probabilities (30.4 and 28.0 per cent) validate the best-fitting results.

The median-filtered results are also combined over the first four FWHMs and the corresponding likelihood is depicted by the dashed curve, resulting in the estimate $f_{\rm NL,C} = 39.8 \pm 34.9$. The point sources lead to an overestimate of $f_{\rm NL,C}^{\rm best}$ at the 0.21σ level according to this comparison. The combined estimators, $\Delta\mathcal{L}_{a,\rm C}(\nu)$, for the KQ75B processed data and $\mathcal{L}_{a,\rm C}^{\rm NG}(\nu,\, f_{\rm NL} = 0, 47.5, 77.5)$[4] for the corresponding $f_{\rm NL}$ simulations are illustrated in Fig. 10 for comparison.

4.2.3 *Cosmic variance and $f_{\rm NL}^{\rm best}$*

It is interesting that $f_{\rm NL}^{\rm best}$s show a monotonic correlation with smoothing scale. The discussions above argue against the explanation based on point sources or goodness-of-fit. We search for this kind of correlation in our mock samples to investigate whether cosmic variance is a possible source of such a correlation. In order to make a comprehensive and reliable interpretation, we pick up those Gaussian and $f_{\rm NL}$ samples which show $f_{\rm NL}$ features at least to the same extent as the *WMAP*5 data. The selection method is introduced below.

(1) *Gaussian samples.* Similar to the *WMAP*5 data, each of the 102 40 Gaussian samples of $\Delta\mathcal{L}_{\rm a}(\nu)$, is input into $f_{\rm NL}$ estimations on all nine FWHMs as introduced in Section 3.2.2. The χ^2 for each FWHM, $\chi^2_{\rm Gauss}\,(f_{\rm NL},\, \theta_{\rm FWHM})$, is obtained as a function of smoothing scale and $f_{\rm NL}$ before we combine the estimators of all nine FWHMs to $\Delta\mathcal{L}_{\rm C}(\nu,\, f_{\rm NL})$. The combined χ^2, $\chi^2_{\rm C,Gauss}\,(f_{\rm NL})$, and likelihood are then computed by the combined estimator. We find 3111 samples whose min $[\chi^2_{\rm C,Gauss}(f_{\rm NL})]$ are less than $\chi^2_{\rm C,min}$ from the *WMAP*5 data. It is believed that these samples demonstrate better $f_{\rm NL}$-like features (of $f_{\rm NL}^{\rm best}$) than the *WMAP*5 data for all nine smoothing scales even though there is no non-Gaussian component encoded in the simulations.

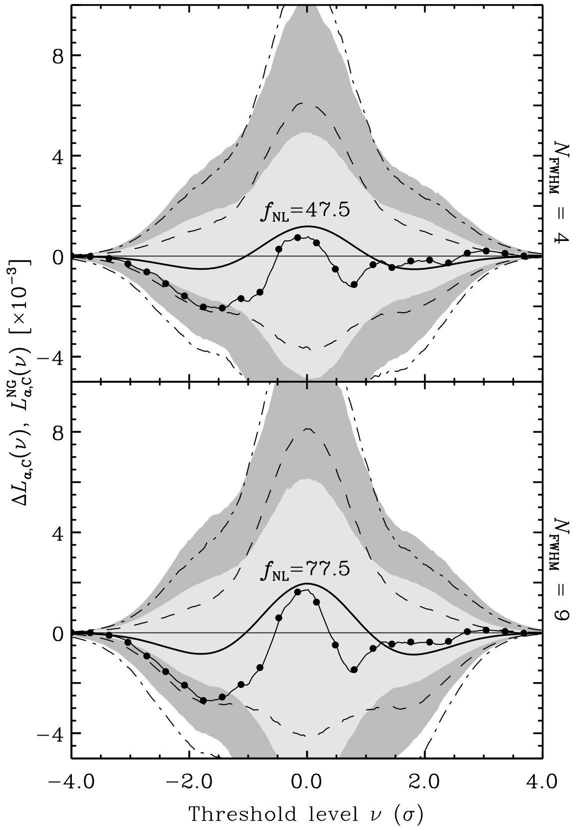

Figure 10. The combined skeleton estimator of the data, Gaussian and non-Gaussian predictions with $N_{\rm FWHM} = 4$ (upper) and 9 (lower). The thin-solid curves show $\Delta\mathcal{L}_{a,\rm C}(\nu)$ of *WMAP*5 data with the filled circles showing the corresponding 25 bins' rebinnings. The grey bands represent the 1σ and 2σ confidence regions of the Gaussian predictions of $\Delta\mathcal{L}_{a,\rm C}(\nu)$. According to 2500 $f_{\rm NL}$ simulations, the thick solid curves depict the expectation of $\mathcal{L}_{a,\rm C}^{\rm NG}(\nu,\, f_{\rm NL} = 47.5,\ 77.5)$ for $N_{\rm FWHM} = 4$ and 9, respectively, and the dashed and dot–dashed curves depict the corresponding 1σ and 2σ confidence boundaries.

(2) $f_{\rm NL}$ *samples.* For the nine FWHM combination discussed in Section 4.2.2, samples with $\chi^2_{\rm C,min}(f_{\rm NL}|f_{\rm NL}^{\rm true} = f_{\rm NL,C}^{\rm best})$ less than the *WMAP*5 $\chi^2_{\rm C,min}$ are selected from 2500 groups of $f_{\rm NL}$ samples. The 701 selected samples form the $f_{\rm NL}$ reference for investigating the correlation between $f_{\rm NL}^{\rm best}$s and smoothing scale.

In 3111 selected Gaussian samples, we find 844 that feature a monotonic correlation with smoothing scale (∼27.1 per cent). Similarly, there are 222 $f_{\rm NL}$ samples from 701 showing the same behaviour (∼31.7 per cent). According to our tests, they show similar properties to that illustrated in the top panel of Fig. 9 where the ML for large-scale smoothing is 'pulled' significantly to the non-Gaussian region. There is a considerable probability (around 30 per cent) of such a correlation so that cosmic variance is a highly probable explanation.

5 CONCLUSIONS

In this paper, we have studied the local approximation to the skeleton on a 2D sphere pixelized in the HEALPIX scheme, and refined the

---

[4] Note that the step-length for $f_{\rm NL}$ sampling is 2.5 in our analysis. $f_{\rm NL} = 47.5$ and 77.5 are the ML values.

method of tracing the quantity. The statistical properties of the skeleton estimator have subsequently been investigated using mock CMB temperature anisotropy maps.

The cubic spline interpolation method locates the skeleton knots more accurately than the simple linear method, which makes the local linear system more robust at the knots. This is of great importance for finer analysis of the local system. For example, the studies on skeleton classification (Pogosyan et al. 2009), which is performed by analysing the eigenvalues of the linear characteristic equation, request highly accurate estimation of such eigenvalues in particular around the demarcation point between two types of skeleton. Our modification provides a more reliable basis for this kind of study. The departure of the skeleton length distribution from its Gaussian expectation shows connections with both the sign and the magnitude of $f_{\rm NL}$ so that it would yield a $f_{\rm NL}$ likelihood function. Based on simulated sets of CMB temperature anisotropy with a local type of non-Gaussian component, it has been tested that both the differential and cumulative skeleton estimators provide unbiased and sufficiently converged likelihood function for $f_{\rm NL}$, but the latter yields a likelihood 10 per cent more converged than the former.

The estimator was applied to the 5-yr *WMAP* data release and the results compared with not only the Gaussian predictions, but also the results from the 1-yr *WMAP* data processing by Eriksen et al. (2004). An $f_{\rm NL}$ likelihood function has been estimated by computing the χ^2 on the basis of 2500 sets of $f_{\rm NL}$ samples. We have also investigated the goodness-of-fit, the impact of the point sources and the comic variance effect on the best-fitting amplitudes of $f_{\rm NL}$. The analysis is carried out on the $V + W$ combined map for various sky coverages.

The processing steps in our analysis follow closely those of Eriksen et al. (2004) but utilize the new 5-yr KQ75 mask and combined V- and W-band data. The smoothing scales adopted in our data processing are also identical to those selected in Eriksen et al. (2004). Our skeleton results show an apparent deviation from the 1-yr ones. According to an extensive series of tests, it is the difference between the two Galactic plane regions defined by the KQ75 and Kp0 masks that contributes mostly to the shifts. Generally, the KQ75 mask excludes a more extended region close to the Galactic plane than the Kp0 mask, and this should be more conservative for temperature analysis. This kind of deviation to the skeleton estimates implies a systematic bias in $f_{\rm NL}$ estimation, in other words, previous $f_{\rm NL}$ studies carried out on Kp0 sky coverage (or even the less conservative KP2 mask) may be biased by the residual Galactic foreground within the dark-grey regions as shown in Fig. 3. We do not exclude the pixels located in point sources to allow sufficient convergence of the likelihood. The impact of the point sources on the estimator is investigated by analysing the difference to samples using median-filtered maps. The results show that the point sources do have an asymmetric impact on the estimator between the positive and negative temperature thresholds on the four smallest smoothing scales. However, the effect is less significant for larger FWHMs. The results of our frequentist analysis show that the *WMAP*5 data are consistent with Gaussian predictions.

We have estimated the $f_{\rm NL}$ likelihoods on nine smoothing levels. The results show an unexpected positive correlation between the best-fitting amplitudes, $f_{\rm NL}^{\rm best}$, and FWHM smoothing scales. The peak of the likelihood function seems to be 'pulled' to a highly non-Gaussian region with the Gaussian case, $f_{\rm NL} = 0$, being 'expelled' to the very tail of likelihood for some large smoothing scales. Further investigations argue against a point source explanation since the median-filtered data still exhibit such a correlation. However, the presence of point sources may yield an overestimation of $f_{\rm NL}^{\rm best}$.

The combination of samples for the first four and all nine smoothing scales lead to the best-fitting amplitudes with 1σ errors, $f_{\rm NL} = 47.3 \pm 34.9$ and 76.8 ± 43.1, respectively. The median-filter studies suggest that the best fit over four scales may be overestimated at the 0.21σ level because of point sources. An investigation has been carried out on the unexpected correlation between $f_{\rm NL}^{\rm best}$s and smoothing scales using both Gaussian and $f_{\rm NL}$ samples with a goodness-of-fit better than that for *WMAP*5. About 30 per cent of them show the behaviour seen in our analysis, so that cosmic variance may be an appropriate explanation for this issue.

ACKNOWLEDGMENTS

ZH acknowledges the support by Max-Planck-Gesellschaft Chinese Academy of Sciences Joint Doctoral Promotion Programme (MPG-CAS-DPP), and some useful discussions with H. K. Eriksen, Jun Pan and Xi Kang. We give special thanks to Stéphane Colombi for suggestions on improving the manuscript. The computations were performed at the Rechenzentrum Garching (RZG) of Max-Planck-Gesellschaft and the GPU cluster of the cosmology group in Purple Mountain Observatory (PMO). Some of the results in this paper have been derived using the HEALPix (Górski et al. 2005) software and analysis package. We acknowledge use of the Legacy Archive for Microwave Background Data Analysis (LAMBDA) supported by the NASA Office of Space Science.

REFERENCES

Bardeen J. M., Steinhardt P. J., Turner M. S., 1983, Phys. Rev. D, 28, 679
Bennett C. L. et al., 1996, ApJ, 464, L1
Bennett C. L. et al., 2003a, ApJS, 148, 1
Bennett C. L. et al., 2003b, ApJS, 148, 97
Bernardeau F., Colombi S., Gaztañaga E., Scoccimarro R., 2002, Phys. Rep., 367, 1
Cabella P., Pietrobon D., Veneziani M., Balbo A., Crittenden R., de Gasperis G., Quercellini C., Vitorio N., 2010, MNRAS, 405, 961
Elsner F., Wandelt B., 2009, ApJS, 184, 264
Eriksen H. K., Novikov D. I., Lilje P. B., Banday A. J., Górski K. M., 2004, ApJ, 612, 64
Gold B. et al., 2009, ApJS, 180, 265
Górski K. M., Hivon E., Banday A. J., Wandelt B. D., Hansen F. K., Reinecke M., Bartelmann M., 2005, ApJ, 622, 759
Guth A. H., 1981, Phys. Rev. D, 23, 347
Hikage C., Komatsu E., Matsubara T., 2006, ApJ, 653, 11
Hikage C., Matsubara T., Coles P., Liguori M., Hansen F. K., Matarrese S., 2008, MNRAS, 389, 1439
Hinshaw G. et al., 2007, ApJS, 170, 288
Jeong E., Smoot G. F., 2007, preprint (arXiv:0710.2371)
Komatsu E., Spergel D. N., 2001, Phys. Rev. D, 63, 063002
Komatsu E., Wandelt B. D., Spergel D. N., Banday A. J., Górski K. M., 2002, ApJ, 566, 19
Komatsu E. et al., 2003, ApJS, 148, 119
Komatsu E., Spergel D. N., Wandelt B. D., 2005, ApJ, 634, 14
Komatsu E. et al., 2009, ApJS, 180, 330
Liguori M., Matarrese S., Moscardini L., 2003, ApJ, 597, 57
Liguori M., Yadav A., Hansen F. K., Komatsu E., Matarrese S., Wandelt B., 2007, Phys. Rev. D, 76, 105016
Matsubara T., 2003, ApJ, 584, 1
Mukhanov V. F., Feldman H. A., Brandenberger R. H., 1992, Phys. Rep., 215, 203
Nolta M. R. et al., 2009, ApJS, 180, 296
Novikov D., Feldman H. A., Shandarin S. F., 1999, Int. J. Modern Phys. D, 8, 291
Novikov D., Colombi S., Doré O., 2006, MNRAS, 366, 1201

Pogosyan D., Pichon C., Gay C., Prunet S., Cardoso J. F., Sousbie T., Colombi S., 2009, MNRAS, 396, 635

Schmalzing J., Górski K. M., 1998, MNRAS, 297, 355

Shandarin S. F., Feldman H. A., Xu Y., Tegmark M., 2002, ApJS, 141, 1

Sousbie T., Pichon C., Courtois H., Colombi S., Novikov D., 2008a, ApJ, 672, L1

Sousbie T., Pichon C., Colombi S., Novikov D., Pogosyan D., 2008b, MNRAS, 383, 1655

Spergel D. N. et al., 2007, ApJS, 170, 377

Yadav A. P. S., Wandelt B. D., 2008, Phys. Rev. Lett., 100, 181301

Yadav A. P. S., Komatsu E., Wandelt B. D., Liguori M., Hansen F. K., Matarrese S., 2008, ApJ, 678, 578

APPENDIX A: THE LOCAL SKELETON IN HEALPIX FRAME

We construct a local coordinate system on the 2D HEALPix sky map shown in Fig. A1, where the direction to the Galactic North Pole is depicted as 'N'. Following the HEALPix coordinate conventions,[5] two orthogonal axes, x and y in equation (3), are set to be aligned with the polar angle θ and azimuth ϕ axes, respectively.

Our starting point is identical with that of Eriksen et al. (2004) in that we determine a pair of vertices on the edge of the pre-constructed secondary pixels on $\mathcal{S}$, with one vertex value lower but the other higher than zero (cancelling vertices, hereafter). It is suggested that the underlying skeleton crosses over those edges connecting pairs of cancelling vertices. Fig. A1 illustrates an exaggerated version of this process. Interpolation is then necessary to determine the positions of the intersections on edges (skeleton knots, hereafter). Linear interpolation has been adopted previously (Novikov, Feldman & Shandarin 1999; Shandarin et al. 2002; Eriksen et al. 2004), since it has been widely employed in morphological studies on both the CMB and large-scale structures, e.g. the length and genus quantities of MFs, which are related to the contour lines of the random fluctuation field and its derivatives. However, the accuracy of an interpolation method is limited by the topological properties of the random field and the pixel size of the corresponding realization. Linear interpolation is accurate enough for an analysis of the MFs at current observational resolutions ($N_{\rm side} = 512$, 1024), however, it is inadequate to provide precise positions of 'knots' on the skeleton map in equation (4) as a higher order (cubic) random field. This may introduce not only bias in to the statistics of the skeleton length for a specific realization, but also could result in a false determination of the eigenvalue of the local linear system, in particular around the demarcation point between the two types of skeletons considered for studies of skeleton classifications (Pogosyan et al. 2009). Given the cubic nature of the skeleton field, we therefore apply a cubic spline interpolation in this analysis, as introduced in the following text in detail. A comparison between the linear and cubic spline strategy is presented in Appendix B.

Once a pair of cancelling vertices has been found, e.g. x_2 and x_3 in Fig. A1, the 6 pixels are then picked up with cancelling vertices in the middle, as $x_0,\ x_1, \ldots,\ x_5$. The connection lines of the 6-pixel centres must cross over the pairs of opposite sides of the quadrangular pixels and be parallel with the connection line of cancelling vertices (e.g. $\overline{x_2x_3}$). The values of these 6 pixels (vertices of secondary pixels), $y_i = \mathcal{S}(x_i) (i = 0, 1, 2, 3, 4, 5)$, are utilized to find the spline functions along the connection lines:

$$\mathcal{S}(x) = \begin{cases} S_0(x) & x \in [x_0, x_1] \\ S_1(x) & x \in [x_1, x_2] \\ \vdots & \vdots \\ S_4(x) & x \in [x_4, x_5] \end{cases}, \tag{A1}$$

where each S_i is the piecewise cubic polynomial between the pixel centres:

$$\begin{aligned} S_i(x) = & \frac{z_{i+1}(x - x_i)^3 + z_i(x_{i+1} - x)^3}{6h_i} \\ & + \left(\frac{y_{i+1}}{h_i} - \frac{h_i}{6} z_{i+1}\right)(x - x_i) \\ & + \left(\frac{y_i}{h_i} - \frac{h_i}{6} z_i\right)(x_{i+1} - x). \end{aligned} \tag{A2}$$

h_i is equal to $|\boldsymbol{x}_{i+1} - \boldsymbol{x}_i|$ corresponding to the radial distance of the 2-pixel centres. The coefficients $\{z_i\}$ can be obtained by solving the linear system

$$\begin{aligned} & h_{i-1} z_{i-1} + 2(h_{i-1} + h_i) z_i + h_i z_{i+1} \\ & \quad = 6\left(\frac{y_{i+1} - y_i}{h_i} - \frac{y_i - y_{i-1}}{h_{i-1}}\right), \quad i = 1, 2, 3, 4 \\ & \quad z_0 = z_5 = 0, \end{aligned} \tag{A3}$$

where y_i corresponds to the pixel value at x_i, i.e. the skeleton value, $\mathcal{S}(x_i)$, in this work.

Note that this six-point system on the sphere has been approximated by a 1D straight line since the pixel size in our analysis is so small ($N_{\rm side} = 1024$, $\theta_{\rm pix} \sim 3.44$ arcmin). In fact, we only need $S_2(x)$ to determine the locations of the knots, e.g. p_3 in Fig. A1, by solving the cubic equation

$$S_2(x) = 0. \tag{A4}$$

There is one and only one real root, x_k, satisfying the condition $x_2 < x_k < x_3$. Then the vector of the underlying knot can be obtained as

$$\boldsymbol{x}_k = \frac{x_3 - x_k}{x_3 - x_2}\boldsymbol{x}_2 + \frac{x_k - x_2}{x_3 - x_2}\boldsymbol{x}_3, \tag{A5}$$

and the corresponding temperature value at $\boldsymbol{x}_k$ is

$$T_k = \frac{x_3 - x_k}{x_3 - x_2} T_2 + \frac{x_k - x_2}{x_3 - x_2} T_3. \tag{A6}$$

According to Fig. A1, after determining the vector of p_2 and p_3 (i.e. $\boldsymbol{x}_{k2}$ and $\boldsymbol{x}_{k3}$), the skeleton length within the secondary pixel, $x_2x_3x'_3x'_2$, can be estimated by the dot product of these two vectors:

$$\delta L(T_{\rm s}) = \arccos\left(\frac{\boldsymbol{x}_{k2}}{|\boldsymbol{x}_{k2}|} \cdot \frac{\boldsymbol{x}_{k3}}{|\boldsymbol{x}_{k3}|}\right). \tag{A7}$$

The corresponding temperature value of this piece of skeleton length, $T_{\rm s}$, is approximately the simple average of T_{k2} and T_{k3}.

It is always the case that the four edges of one secondary pixel are connecting cancelling vertices. Most of these cases indicate a stationary point (maxima or minima or saddle point) within this secondary pixel, implying two skeletons cross inside. There are still a few exceptions but they will become very rare due to the small pixel size and the smoothing applied afterwards. We therefore make the same assumption as in Eriksen et al. (2004) that all of the cases indicate a pair of skeletons crossing over each other. The possible deviation from the length distribution is totally negligible according to various tests.

---

[5] see 'The HEALPix Primer' in software package, version 2.10.

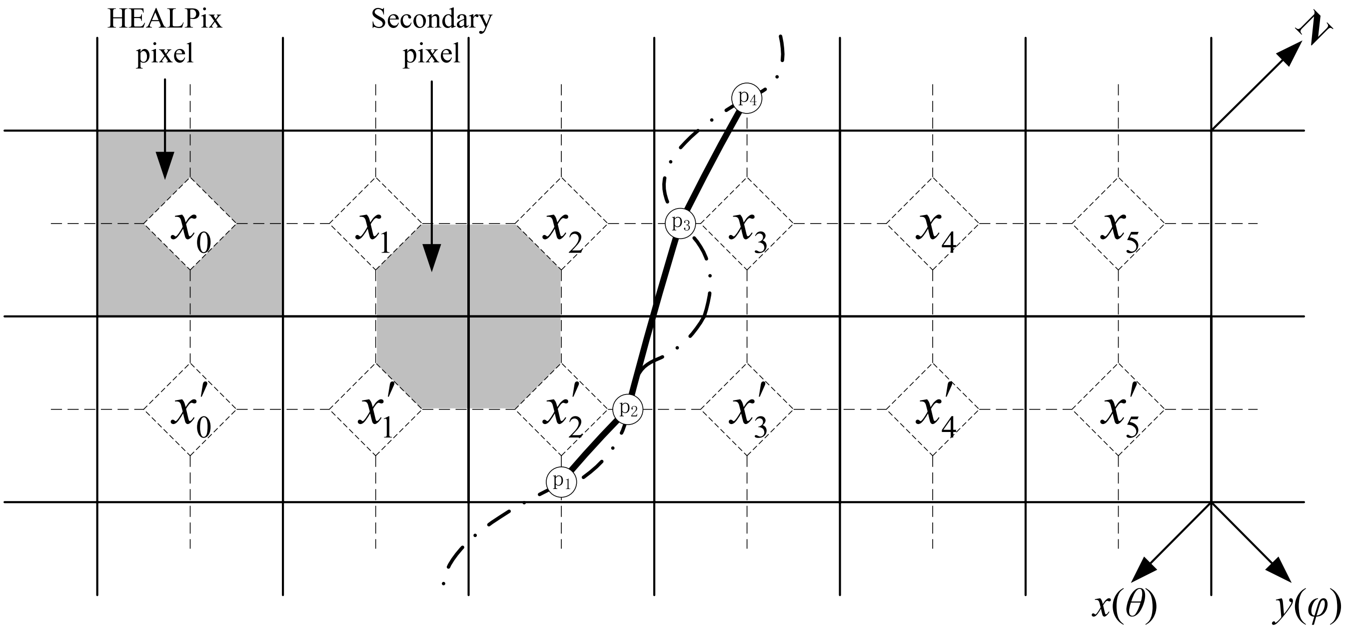

Figure A1. Tracing the underlying contour (dot–dashed curve) on the grid of the HEALPix pixelization scheme. The x_i mark the positions of the primary pixels utilized in the cubic spline interpolation (equations A1 and A2). The thick solid lines connect the estimated intersection points (p_is) between the underlying contour and the edge of the secondary pixels by means of a cubic spline interpolation. The definition of secondary pixels is identical to that of Eriksen et al. (2004). We select a coordinate system consistent with the HEALPix convention, which is specified by a north direction, 'N', and two orthogonal directions (θ, ϕ) for derivative.

APPENDIX B: COMPARISON BETWEEN LINEAR AND CUBIC SPLINE INTERPOLATION FOR SKELETON ANALYSIS

On a pixelized 2D random field, the key step in tracing the local skeleton is to locate the skeleton knot which is always within the line connecting the centres of the two cancelling neighbouring pixels (one edge of the secondary pixel), and whose position is conventionally estimated by linear interpolation, since the skeleton realization $\mathcal{S}$ can be considered as a linear function along the line connecting just a few pixels at a very high resolution level. This is an approximation that makes things easier to handle, especially for the HEALPix pixelization scheme. However, the skeleton is actually a cubic function, so that it is necessary to test whether linear interpolation is sufficient for its computation. In this appendix, we investigate the linear properties at the skeleton knots derived by linear and cubic spline interpolation methods.

The characteristic equation (equation 2) for the 2D random field must be satisfied at the skeleton knots. It can be re-expressed for a CMB temperature field as

$$\begin{pmatrix} T_{;\theta\theta} & T_{;\theta\phi} \\ T_{;\phi\theta} & T_{;\phi\phi} \end{pmatrix} \begin{pmatrix} T_{;\theta} \\ T_{;\phi} \end{pmatrix} = \lambda \begin{pmatrix} T_{;\theta} \\ T_{;\phi} \end{pmatrix}. \tag{B1}$$

We define

$$r_1 \equiv \frac{T_{;\theta\theta}T_{;\theta} + T_{;\theta\phi}T_{;\phi}}{T_{;\theta}}, \quad r_2 \equiv \frac{T_{;\phi\theta}T_{;\theta} + T_{;\phi\phi}T_{;\phi}}{T_{;\phi}},$$

and λ should satisfy the following:

$$\begin{vmatrix} T_{;\theta\theta} - \lambda & T_{;\theta\phi} \\ T_{;\phi\theta} & T_{;\phi\phi} - \lambda \end{vmatrix} = 0 \tag{B2}$$

with two real roots λ_1 and $\lambda_2 (\lambda_1 \geq \lambda_2)$. In principle, r_1 should be equal to r_2 and also equal to λ_1 or λ_2 along the underlying skeleton. However, in practice, we have to investigate such a property at the position of the estimated skeleton knots on the pixelized sphere where r_1 and r_2 are not exactly equal because of estimation errors. The first and second derivatives there can be obtained safely by linear interpolation as in equation (A6). We define a new quantity $r \equiv (r_1 + r_2)/2$. The numerical robustness of the equivalence between r and λ indicates the quality of the estimation method.

In this test, we pick up two 6-pixel arrays $(x_0, x_1, \ldots, x_5)$ from one simulated Gaussian realization (resolution parameter $N_{\rm side} = 1024$) smoothed by Gaussian beams with FWHM = 30 and 60 arcmin. The pixel location of the two arrays is exactly the same with each other. The corresponding values of $\mathcal{S}$ in equation (4) are marked by filled triangles in Fig. B1. For the case of FWHM = 30 arcmin, $x_2\,x_3$ is a pair of cancelling pixels and P_f point (P point) is the estimated skeleton knot determined by a linear (cubic spline) interpolation method. The linear properties at the two points are quantified as

$$\begin{aligned} P_f :\ & r_1 = -0.6887, \quad r_2 = -0.7466, \quad r = -0.7174, \\ & \lambda_1 = -0.6422, \quad \lambda_2 = -0.7221, \\ P :\ & r_1 = -0.7099, \quad r_2 = -0.7116, \quad r = -0.7108, \\ & \lambda_1 = -0.6125, \quad \lambda_2 = -0.7107 \quad \text{(secondary skeleton)}. \end{aligned}$$

It is shown in this example that the cubic spline interpolation leads to a more accurate location of the skeleton knots, and the distribution of skeleton length therein. Note that there are two suspicious skeleton knots within x_3 and x_4 in this case but they would not be involved in analysis since x_3 and x_4 are not cancelling pixels. It is also noteworthy that the point P belongs to a piece of the first-type secondary skeleton according to the classification in Pogosyan et al. (2009). The robust equivalence between r and the eigenvalue indicates accurate and unbiased classification, in particular around the underlying demarcation point between two types of skeleton where the two eigenvalues are quite close to each other. The cases for

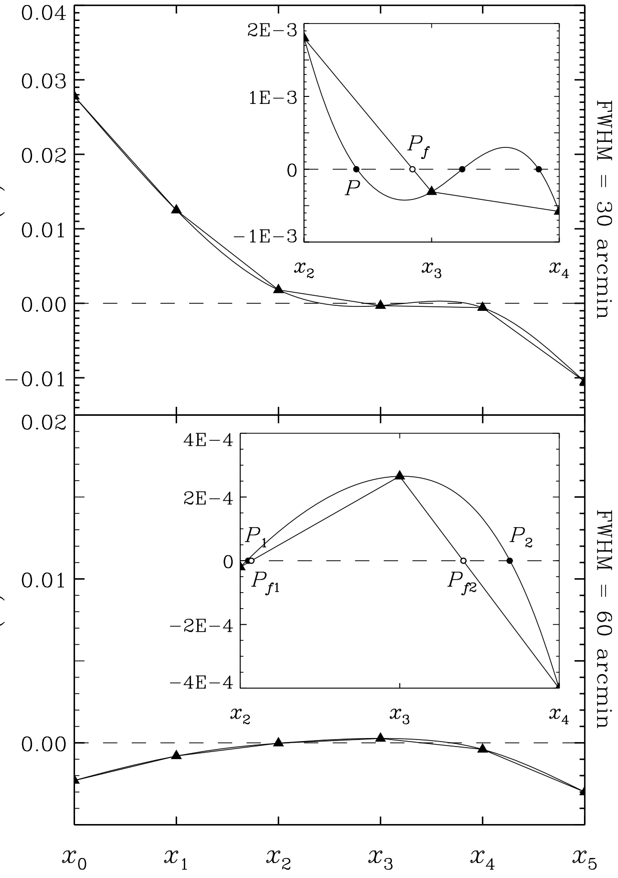

Figure B1. The pieces of profile of $\mathcal{S}$ within a 6-pixel array reproduced by linear and cubic spline interpolation from *one* Gaussian simulation. The centres of the 6 pixels are identified by $x_0, x_1, \ldots, x_5$ where the values of $\mathcal{S}$ are marked by filled triangles. The positions of the skeleton knots estimated by cubic splines (linear lines) are located by the filled (open) circles. The small plots inside zoom the curves within x_2 and x_4. The pixel index (position) of x_i is selected to be the *same* for FWHM = 30 and 60 arcmin.

FWHM = 60 arcmin are listed below:

$$P_{f1}:\ r_1 = 0.0428,\quad r_2 = -0.4198,\quad r = -0.2313,$$
$$\lambda_1 = -0.2114,\quad \lambda_2 = -0.8062,$$
$$P_1:\ r_1 = -0.1916,\quad r_2 = -0.2425,\quad r = -0.2170,$$
$$\lambda_1 = -0.2108,\quad \lambda_2 = -0.8060 \text{ (primary skeleton)},$$

$$P_{f2}:\ r_1 = -0.9264,\quad r_2 = -0.7597,\quad r = -0.8430,$$
$$\lambda_1 = -0.2230,\quad \lambda_2 = -0.8091,$$
$$P_2:\ r_1 = -0.7981,\quad r_2 = -0.8004,\quad r = -0.7993,$$
$$\lambda_1 = -0.2588,\quad \lambda_2 = -0.7996 \text{ (secondary skeleton)}$$

For the difference between the 5- and 1-yr skeleton processing, we must investigate the impact of method selection on the results. Given the KQ75B processed data and Gaussian simulations, we carry out the skeleton analysis following the steps described in Section 3.2 but utilizing linear interpolation to locate the skeleton knots. The resulting length departure of the data is then obtained

$$\Delta\mathcal{L}^{\rm lin}_{\rm a,WMAP5} = \mathcal{L}^{\rm lin}_{\rm a,WMAP5} - \left\langle \mathcal{L}^{\rm G,lin}_{\rm a} \right\rangle \qquad \text{(B3)}$$

and the differences between the cubic spline and linear results are plotted in Fig. B2 for FWHM = $0^{\circ}\!.53$, $0^{\circ}\!.64$, $0^{\circ}\!.85$ and $1^{\circ}\!.28$. It is noteworthy that the magnitude of such a difference contributes less than 10 per cent to the discrepancy between the *WMAP*5 and *WMAP*1 skeleton length distribution profile. However, the structure shown in Fig. B2 suggests that the linear method would lead to an overenhanced peak and overdepressed trough, which for the positive $f_{\rm NL}$ structure of $\Delta\mathcal{L}_{\rm a}$ suggested by the data may bias the best-fitting value of $f_{\rm NL}$.

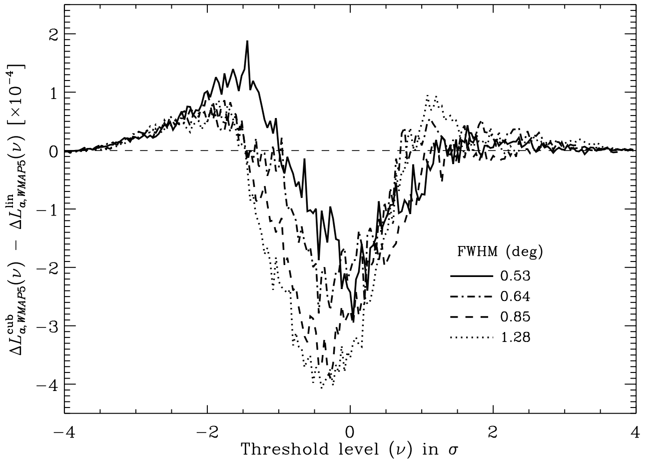

Figure B2. The difference of $\Delta\mathcal{L}_{\rm a}$ of *WMAP*5 data between the cubic spline (cub) and linear (lin) interpolation processing. The cases of different smoothing scales are distinguished by different line styles.

APPENDIX C: TEST OF THE LIKELIHOODS FROM THE COMBINED ESTIMATOR

In this section we test for the presence of bias in our combined estimator. Given simulated noisy realizations from the KQ75B processing and the predetermined expectation $\langle \mathcal{L}^{\rm NG}_{\rm C}(\nu, f_{\rm NL})\rangle$, we randomly pick up $N = 250$ sets of $f_{\rm NL}$ samples, $\mathcal{L}^{\rm NG}_{\rm C}(\nu, f^{j}_{\rm NL})(j = 1, 2, \ldots, 250)$ with $N_{\rm FWHM} = 4$ and 9, to form the conditional χ^2

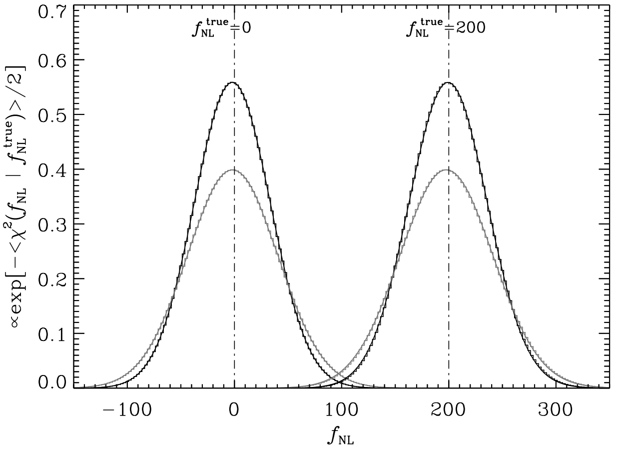

Figure C1. $\exp[-(1/2N)\sum_{j=1}^{N}\chi^2(f^{j}_{\rm NL}|f^{\rm true}_{\rm NL})]$, the effective likelihood functions computed by the combined accumulative estimator $\mathcal{L}^{\rm NG}_{\rm a,C}$ from KQ75B processed noisy simulations with input parameter $f^{\rm true}_{\rm NL} = 0$, 200. The functions are renormalized by different factors for visual convenience and are shown by histograms. The Gaussian-fitting functions are depicted by solid curves. The higher, narrower (lower, wider) histograms and curves correspond to the combinations with $N_{\rm FWHM} = 4$ (9).

functions

$$\chi^2_{\mathrm{C}}\left(f^j_{\mathrm{NL}}|f^{\mathrm{true}}_{\mathrm{NL}}\right) = \sum_{\nu}\left\{\frac{\mathcal{L}^{\mathrm{NG}}_{\mathrm{C}}\left(\nu, f^j_{\mathrm{NL}}\right) - \left\langle\mathcal{L}^{\mathrm{NG}}_{\mathrm{C}}\left(\nu, f^{\mathrm{true}}_{\mathrm{NL}}\right)\right\rangle}{\sigma\left[\mathcal{L}^{\mathrm{NG}}_{\mathrm{C}}\left(\nu, f^{\mathrm{true}}_{\mathrm{NL}}\right)\right]}\right\}^2 \quad \text{(C1)}$$

and the effective likelihood function for each sample,

$$\mathscr{L}_{\mathrm{C}}\left(f_{\mathrm{NL}}|f^{\mathrm{true}}_{\mathrm{NL}}\right) \propto \exp\left[-\frac{1}{2N}\sum_{j=1}^{N}\chi^2_{\mathrm{C}}\left(f^j_{\mathrm{NL}}|f^{\mathrm{true}}_{\mathrm{NL}}\right)\right]. \quad \text{(C2)}$$

We plot $\mathscr{L}_{\mathrm{C}}(f_{\mathrm{NL}}|f^{\mathrm{true}}_{\mathrm{NL}})$ as histograms for two given $f^{\mathrm{true}}_{\mathrm{NL}}$ values (0 and 200) in Fig. C1 for $N_{\mathrm{FWHM}} = 4$ and 9, noticing that the sampling width Δf_{NL} is 2.5. Again, the likelihoods are perfectly fitted by Gaussian functions with the parameters listed in Table C1. Despite the noise contribution and sky cut, it is demonstrated that the inverse-variance combination still leads to an unbiased skeleton estimator for f_{NL}.

Table C1. The ML ($f^{\mathrm{ML}}_{\mathrm{NL}}$), best-fitting ($f^{\mathrm{best}}_{\mathrm{NL}}$) values and 1$\sigma$ error from the likelihood $\mathscr{L}_{\mathrm{C}}(f_{\mathrm{NL}}|f^{\mathrm{true}}_{\mathrm{NL}})$ (Fig. C1) computed from the combined estimator derived from $N = 250$ KQ75B processed noisy simulations with given parameter $f^{\mathrm{true}}_{\mathrm{NL}} = 0,\ 200$.

N_{FWHM}	$f^{\mathrm{true}}_{\mathrm{NL}}$	$f^{\mathrm{ML}}_{\mathrm{NL}}$	$f^{\mathrm{best}}_{\mathrm{NL}}$	$\sigma_{f_{\mathrm{NL}}}$
4	0.0	−2.5	−2.0	35.5
9	0.0	−2.5	−1.7	42.3
4	200.0	200.0	199.4	36.5
9	200.0	197.5	197.8	43.4

This paper has been typeset from a TEX/LATEX file prepared by the author.